



Power Electronic Systems
Laboratory

© 2022 IEEE

IEEE Transactions on Power Electronics, Vol. 38, No. 2, pp. 2307-2326, February 2023

100 kHz Large-Signal Bandwidth GaN-Based 10 kVA Class-D Power Amplifier with 4.8 MHz Switching Frequency

P. Niklaus,
J. W. Kolar,
D. Bortis

Personal use of this material is permitted. Permission from IEEE must be obtained for all other uses, in any current or future media, including reprinting/republishing this material for advertising or promotional purposes, creating new collective works, for resale or redistribution to servers or lists, or reuse of any copyrighted component of this work in other works



Eidgenössische Technische Hochschule Zürich
Swiss Federal Institute of Technology Zurich

100 kHz Large-Signal Bandwidth GaN-Based 10 kVA Class-D Power Amplifier with 4.8 MHz Switching Frequency

Pascal S. Niklaus, *Student Member, IEEE*, Johann W. Kolar, *Fellow, IEEE*, and Dominik Bortis, *Senior Member, IEEE*

Abstract—Power Amplifiers (PAs) are widely used, for example, to emulate the behavior of the power grid or electric machines under critical operating conditions, to measure the impedance of the power grid, or to generate specific impedance profiles in Power-Hardware-in-the-Loop (P-HIL) tests. To accurately emulate dynamic effects and to characterize power electronic systems featuring Wide-Bandgap (WBG) power semiconductors, PAs with very high output voltage quality and ever higher Bandwidth (BW) at full output power are required, motivating the development of Ultra-High Bandwidth Power Amplifiers (UHBW-PAs). While linear UHBW-PAs achieve very high signal fidelity and BW, they suffer from a tremendously bad efficiency, demanding large cooling effort and resulting in uneconomical operation, particular at high power levels and/or during long-term tests. Therefore, this paper investigates possibilities for a switch-mode realization of UHBW-PAs with significantly higher efficiency and power density compared to existing solutions. There are two key concepts, namely series- and parallel-interleaving of multiple switching and/or converter cells, that allow to increase the *effective* switching frequency relevant to output filtering without increasing the individual device switching frequency that determines the per device switching losses. This paper analyzes comprehensively the advantages and disadvantages of a combination of series- and parallel-interleaving in terms of losses, volume and complexity scaling. Finally, a UHBW-PA with 10 kVA output power (single-phase), a nominal rms output voltage of 230 V, a full-power BW of 100 kHz, very high output voltage quality (3rd and 5th harmonic < 2.5 V and < 1.2 V, respectively), an efficiency > 95 %, a power density of 25 kW/dm³ (410 W/in³), and a switching frequency of 4.8 MHz is presented. A hardware demonstrator is built and extensive measurements verify the system performance and confirm the calculation from the initial analyses with loss models.

Index Terms—Power amplifiers, Inverters, Power electronics, DC-AC power conversion, Power system testing, wide-bandgap semiconductors, Power-hardware-in-the-loop

I. INTRODUCTION

TESTING and characterization of power electronic systems is of great importance for their stable and reliable operation in the field. In industrial practice, Power-Hardware-in-the-Loop (P-HIL) test environments are mostly used for this purpose, since they offer a cost-effective way to test various operating modes, difficult to achieve with fully implemented

Initial results from this paper were presented in part at the International Conference on Renewable Energy Research and Applications (ICRERA), Brasov, Romania, Nov. 2019. (*Corresponding Author: Pascal S. Niklaus*)

P. S. Niklaus, J. W. Kolar and D. Bortis are with the Power Electronic Systems Laboratory, Swiss Federal Institute of Technology, Zurich 8092, Switzerland (e-mail: niklaus@lem.ee.ethz.ch; kolar@lem.ee.ethz.ch; bortis@lem.ee.ethz.ch).

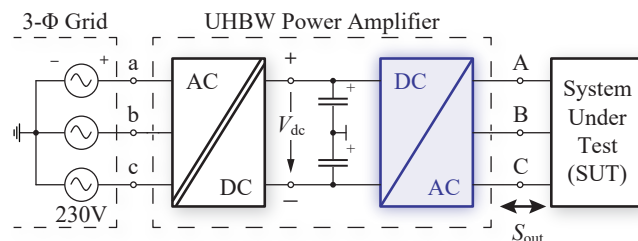


Fig. 1. System overview of the 100 kHz large-signal bandwidth power amplifier. Figure taken from [10].

TABLE I. Main system specifications for one single-phase of the investigated power amplifier.

Parameter		Value
Peak Output Voltage per Phase	$V_{\text{out,pk}}$	0 ... 350 V
Output Frequency	f_{out}	DC ... 100 kHz
Output Power per Phase	S_{out}	0 ... 10 kVA
DC Link Voltage	V_{dc}	800 V
Effective Switching Frequency	$f_{\text{sw,eff}}$	4.8 MHz
System Efficiency (Nom. Op. Pt.)	η	95 %

hardware setups [1]. Here, the behavior of a system model is emulated by means of a Real Time Simulator (RTS) and a Power Amplifier (PA), where the latter is connected to a power electronic System Under Test (SUT) [2], [3]. Examples are the emulation of the power grid for testing grid-tied inverter stages (e.g. photovoltaic inverters) or rectifiers with regard to grid compatibility (voltage imbalances, transient phenomena and/or frequency deviations) [4], the emulation of a certain virtual grid impedance [5], [6], or any dc or ac load, e.g., an electrical machine [7], for analyzing drive systems and/or their control loops. A further application scenario is the measurement of the grid impedance [8], which has a significant impact on the stability of grid-tied converters [9]. As shown, e.g., in [2], the Bandwidth (BW) of such power amplifiers is the ultimate limiting factor for the achievable accuracy when emulating dynamic effects like voltage and/or load transients. Furthermore, maximum output voltage quality, i.e., minimum distortion and minimum noise, must be ensured while simultaneously offering the ability to source and/or sink multiple kVAs of output power (bidirectional power flow, arbitrary load phase angle φ). This clearly motivates the use of Ultra-High Bandwidth Power Amplifiers (UHBW-PAs) as an interface to the SUT. **Fig. 1** shows a very simplified block diagram of such a three-phase UHBW-PA that is composed of a (typically isolated) three-phase grid interfacing rectifier

stage to provide a (galvanically isolated) dc link voltage V_{dc} for the subsequent ultra-high BW inverter stage (dc/ac stage, highlighted in blue). The design of one single-phase module of the latter is the focus of this article. A full three-phase system can then easily be assembled with three such modules. Note that within this article the terms UHBW-PA and PA (used interchangeably) refer to a single-phase module of the highlighted dc/ac stage from **Fig. 1** with the specifications listed in **Table I**. In the nominal operating point, the full 10 kVA output power (per phase) is delivered for a nominal rms output voltage of 230 V at a fundamental frequency of 100 kHz into an ohmic load ($S_{out} = P_{out} = 10 \text{ kW}$). Note that with “large-signal BW” we refer to the frequency at which the amplifier can provide its full-scale output power (at nominal output voltage and current) according to **Table I**, as defined in [11].

Traditionally, such PAs are implemented as linear power amplifiers, especially those with very high BW requirements [12], [13]. While they offer a very high output voltage quality, a major disadvantage of such solutions is their low efficiency (in particular for non-resistive loads and for power *sinking*), which is especially concerning for high output powers and/or long-term tests. Besides the inefficient operation, the high losses demand a large cooling effort and consequently lead to a low power density. For high output powers, switch-mode amplifiers (Class-D amplifiers) are therefore clearly preferred and are also increasingly found in commercial implementations [14], [15]. However, as explained later, to reach the desired output BW in a switch-mode PA, very high switching frequencies in the multi-MHz range are required.

In [11], different implementation options for such switch-mode PAs are presented and their advantages and disadvantages are compared with those of linear and hybrid PAs. Furthermore, a comprehensive review of currently available and developed PAs in industry and academia is given and a switch-mode realization composed of multiple cascaded (series-connected) full-bridges that achieves the same full-power BW of 100 kHz and same single-phase output power of 10 kW is presented. The cascade/series-connection of complete converter cells (full-bridges), denoted Cascaded H-Bridge (CHB) converter, enables an increased *effective* switching frequency and reduced switch-node voltage steps, which is advantageous for output filtering. There are other PA designs realized as CHB converter that achieve remarkable performance, such as [16], a Magnetic Resonance Imaging (MRI) high-power gradient PA with 7 kHz large-signal BW, an output capability of 1000 V/500 A, extremely low noise and high precision resulting from a sophisticated control method, or [17], a 41 level pulsed-sine generator with an output fundamental frequency of up to 1 MHz at an output voltage of up to 2 kV peak-to-peak used for cancer treatment in biomedical applications (output power and output signal quality unspecified). Similarly, [18] demonstrates a CHB based converter with a 1 MHz, 200 V amplitude sinusoidal output with a maximum power of 1.35 kW. The downside common to all CHB realizations, despite their very promising dynamic performance especially under aggressive load conditions and their full modularity (limited output voltage/power might still be available in case

of failure of one CHB cell), is, however, the need for a galvanically isolated dc supply for each converter cell and the resulting relatively large coupling capacitances towards Protective Earth (PE), which cause significant Common Mode (CM) currents. These CM currents must be adequately filtered in order to not impair the converter operation.

A further interesting concept are hybrid analog/digital PA realizations that combine a high power, high efficiency switch-mode PA (main amplifier) with a relatively low power (yet high voltage or high current capable) linear PA (correction amplifier) to achieve maximum output BW and/or maximum signal fidelity/precision and yet moderate system efficiency. They can be seen as compromise between purely analog and fully digital implementations. There are three possible configurations, namely series- and parallel-connection and envelope tracking, which are comprehensively reviewed in [19]. In [20], [21], a CHB based main amplifier is connected in series to a linear correction amplifier in a way that the closed-loop dynamics are determined solely by the latter. Thereby, a BW of 105 kHz of the linear amplifier is achieved, which, e.g., allows to generate full-scale test signals of up to 60 kHz with the hybrid PA. An example of a parallel hybrid PA is shown in [22], where the linear amplifier defines the output voltage and the via a single filter inductor coupled switch-mode amplifier delivers the bulk load current. In that sense, the linear amplifier can be seen as active filter of the switch-mode main amplifier. Similarly, the linear amplifier could be replaced by a low power, fast switching (and therefore, high BW) digital converter, shown, e.g., in [23], [24]. Envelope tracking is a technique where a switch-mode converter forms a varying supply voltage for the linear PA based on the desired output voltage envelope, in order to minimize the voltage drop across and hence the conduction losses in the linear power transistors [25]. A particularly interesting application field are Radio-Frequency (RF) power amplifiers where an RF signal with varying amplitude envelope has to be amplified. Realizations of such an envelope tracking PA based on a three-level buck converter are presented in [26], [27] where experimental results verify accurate tracking of a 10 kHz rectified sine wave with an amplitude of 4 V. A boost-type solution for higher operating voltages (up to 130 V rms) and power levels (up to 1.5 kW) and a tracking BW of 1 kHz is shown in [28].

In contrast to CHB converter cells and/or hybrid analog/digital and digital/digital approaches, which typically are more complex in realization, this article discusses the realization of an entirely switch-mode PA with multiple Switching Cells (SCs) connected in parallel and series, which, in addition to reducing the switch-node voltage steps, also allows an increase in the *effective* switching frequency [29]. Within this article we use the term *Switching Cell* for one half-bridge with corresponding dc link capacitor, unlike CHB *Converter Cells*, which are composed of one full-bridge with dedicated dc link capacitor. The aim is to explore the performance limitations by pushing the (effective) switching frequency to very high values, while still keeping circuit complexity at a reasonable level. In [10], the optimal number of parallel- and series-connected SCs for the specifications given in **Table I** has

already been discussed. In this article, this analysis is extended and verified using a hardware demonstrator.

Section II derives the circuit topology, focusing on semiconductor loss scaling depending on the number of series- and parallel-interleaved SCs and ultimately a suitable topology is selected. **Section III** then shows a detailed design procedure for the High-Frequency (HF) output filter inductors before **Section IV** presents the realized hardware demonstrator of the UHBW-PA including a liquid cooling system and highlights important design aspects. The performance of the hardware demonstrator is experimentally verified in **Section V**. Finally, **Section VI** concludes this article.

II. CONVERTER TOPOLOGY

A. Switch-Mode Power Amplifier

The BW of switch-mode PAs is limited by the necessary output filter (typically a k -stage second-order LC filter with corner frequency f_c and an attenuation of $-k \cdot 40$ dB/dec), which attenuates the HF spectral content in the switched output voltage, such that the local average (averaged over one switching period T_{sw}) remains [22]. This local average is tracking a programmed reference voltage/waveform v_{ref} given by the desired application scenario (e.g., coming from the RTS in P-HIL test environments). Within this article we restrict the discussion to single-stage LC output filters. Assuming a naturally sampled (continuous) Pulse Width Modulation (PWM) with a triangular carrier and a purely sinusoidal v_{ref} with frequency f_{out} , the switched voltage v_{sw} contains spectral components at multiples of the switching frequency $n \cdot f_{sw}$ and the respective sidebands $n \cdot f_{sw} \pm k \cdot f_{out}$ with $n \in \mathbb{N}$ and $k \in \{2, 4, \dots\}$ if n is odd or $k \in \{1, 3, \dots\}$ if n is even [30]. To attenuate sidebands at frequencies below f_{sw} , the filter corner frequency f_c must be substantially lower than f_{sw} . To account for effects such as finite filter slopes (e.g., -40 dB/dec) and component tolerances, in practice, $f_c < f_{sw} / 10$ is typically chosen [31]. At the same time, f_c must be higher than the maximum anticipated output frequency $f_{out,max}$ to avoid exciting the filter resonance ($f_c \geq k_f \cdot f_{out,max}$). Thereby, to reach the desired BW of 100 kHz, switching frequencies in the range of several MHz are required ($f_{sw} \geq 10 \cdot k_f \cdot f_{out,max}$).

The authors of [11] derived the minimum required f_{sw} to reach a certain output voltage quality (quantified by means of the output voltage peak-to-peak ripple $\Delta v_{out,pp}$) for a certain maximum capacitive current and maximum inductive voltage drop in the respective filter elements. For a practical case of $\Delta v_{out,pp} = 2\% \cdot \hat{v}_{out}$ (peak full-scale output voltage \hat{v}_{out}), 30% capacitive current and 15% inductive voltage drop a standard 2-level (2L) Voltage Source Inverter (VSI) requires $f_{sw} = 5$ MHz. Even with the ever more widespread availability of Wide-Bandgap (WBG) power semiconductors with significant reduction of switching losses compared to their traditional Silicon (Si) counterparts, f_{sw} in normal 2L operation is still limited by the (hard) switching losses, particularly if a certain efficiency (95% in the case at hand) is targeted. Therefore, alternative circuit topologies to the 2L-VSI are required, which allow to increase the *effective*

switching frequency $f_{sw,eff}$ of the switched voltage seen by the output filter without the penalty of high switching losses per device (switching losses distributed between multiple devices), i.e., the individual devices switch at a much lower frequency f_{sw} .

Based on results of a previous study on this topic in [10], we briefly repeat the basic idea of series- and parallel-interleaving to ultimately find the most suitable combination of both approaches, i.e., a series-parallel-interleaved multi-level converter topology, which best fulfills the design goals (cf. **Table I**).

1) Series Interleaving:

Multi-level converters are used to increase the number of voltage levels of v_{sw} that is applied to the output filter inductor by phase-shifting the operation of $(M - 1)$ series-connected SCs or full converter cells. Each cell is operated with f_{sw} , generating M distinct voltage levels at the switch-node as depicted in **Fig. 2 (a.ii)-(a.iii)**. The HF harmonics of v_{sw} are shifted to higher frequencies, i.e., to $f_{sw,eff} = (M - 1) \cdot f_{sw}$. Furthermore, the blocking voltage stress of the switches is reduced to $V_{dc} / (M - 1)$, which on the one hand renders certain semiconductor technologies usable in application scenarios where they normally cannot be used (e.g., 600 V Gallium Nitride (GaN) devices with an 800 V dc link) and on the other hand offers the possibility to use lower voltage devices with a potentially better Figure-of-Merit (FOM) [32]. From the various multi-level topologies described in literature, such as Modular Multi-Level Converters (MMCs) [33] (which need active control of the individual submodule capacitor voltages [34]), CHB [35] and Neutral-Point Clamped (NPC) converters [36], [37], the Flying Capacitor Converter (FCC) initially proposed in [38] and depicted in **Fig. 2 (a.i)** has the fundamental advantage that it can generate a high number of voltage levels with reasonable semiconductor effort, lower circuit complexity compared to other multi-level approaches and is capable of generating a dc output without auxiliary circuits for active voltage balancing of the stacked dc link capacitors. It has to be mentioned, however, that under certain operating and load conditions (e.g., low inductor current ripple and dc output voltage component), active balancing of the Flying Capacitor (FC) voltages is required and can be implemented with relatively simple control algorithms, such as the one presented in [26]. As mentioned in the introduction, there are several application scenarios where CHB converters are very well suited but due to circuit complexity and overall system efficiency considerations (an isolated dc link voltage needs to be provided to each individual CHB cell), the FCC is identified as a most promising converter candidate for the given application. The operation of the M -level FCC has been widely discussed in literature [39]–[41] and a further explanation is omitted here.

2) Parallel Interleaving:

High current ratings demand an increased semiconductor area, which can either be realized with large devices or by paralleling N small devices. In the latter case, phase-shifted operation of N parallel-interleaved 2L SCs as shown in **Fig. 2 (b.i)**, hereinafter called branches, can favorably be used (commonly also referred to as multi-phase operation in literature) [42].

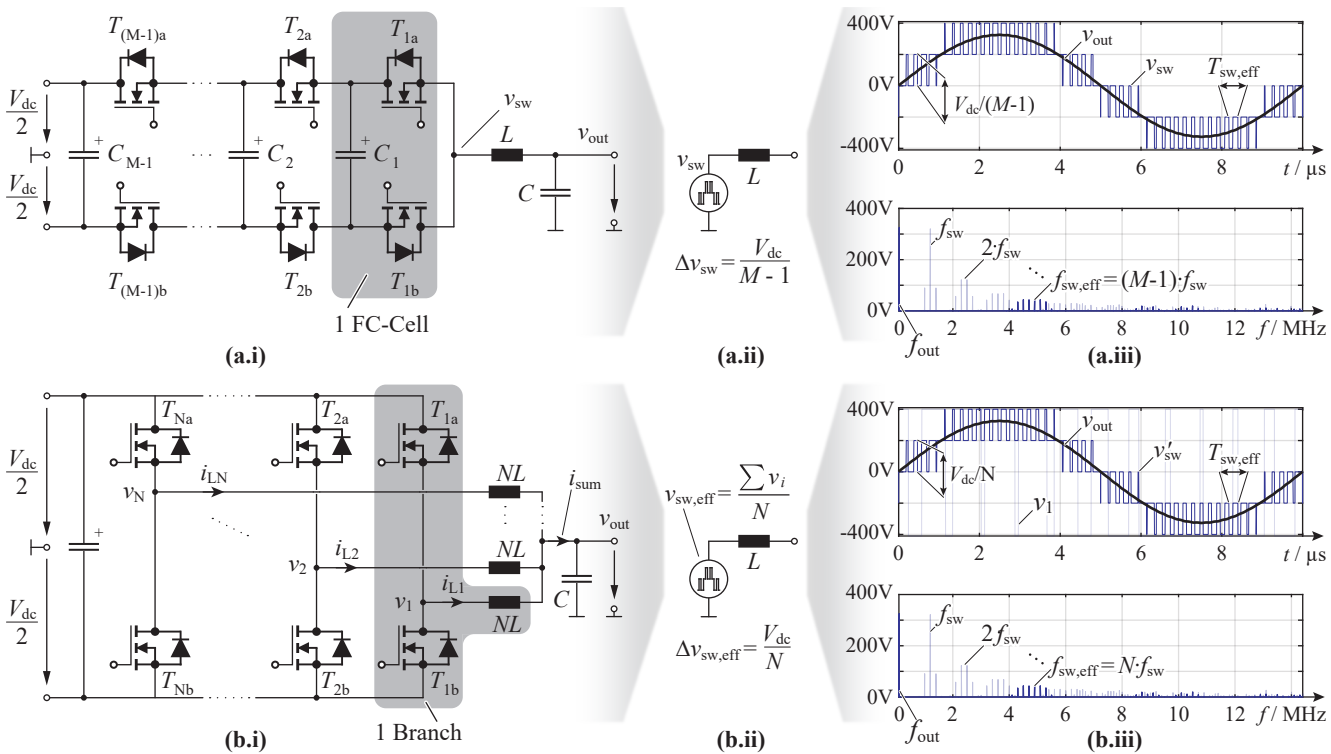


Fig. 2. (a.i) Circuit diagram of an M -level Flying Capacitor Converter (FCC) with one FC-cell highlighted, (a.ii) resulting equivalent circuit for the switch-node voltage v_{sw} and (a.iii) corresponding time- and frequency-domain representations of v_{sw} for $M = 5$, i.e., a 5-level converter (4 FC cells), clearly indicating the multi-level nature of the output voltage with the first occurring frequency component (above f_{out}) in the spectrum at the effective switching frequency $f_{sw,eff} = (M - 1) \cdot f_{sw}$. (b.i) Parallel interleaving of multiple (N) two-level (2L) branches leading to (b.ii) the equivalent circuit with the effective switch-node voltage $v_{sw,eff}$ formed with the inductive voltage divider. The same multi-level waveform (b.iii) as for (a.iii) is achieved by taking the mean of all individual switch-node voltages and thus the first frequency component (above f_{out}) in the spectrum is located at $f_{sw,eff} = N \cdot f_{sw}$ (here shown for 4 interleaved 2L branches); Figure taken from [10].

Not only does this lead to a (partial) cancellation of the current ripple between the individual branches, and hence a reduction of the ripple in the summed output current i_{sum} seen by the filter capacitance C , but at the same time, an increased effective switching frequency $f_{sw,eff} = N \cdot f_{sw}$ is obtained at the output capacitor as illustrated in Fig. 2 (b.ii)-(b.iii) [43]. There, f_{sw} denotes the switching frequency of each individual 2L SC and N the number of interleaved branches. The *effective* (or *virtual*) switch-node voltage $v_{sw,eff}$ results from the inductive voltage divider and shows a multi-level nature that is equal for both, one single series-interleaved M -level bridge leg and $N = M - 1$ times parallel-interleaved two-level half-bridges (cf. Fig. 2 (a.ii) and (b.ii) for $M = 5$ and $N = 4$, respectively). In both cases the voltage spectrum contains no components between f_{out} and $f_{sw,eff}$ (assuming natural sampling PWM), and therefore, the filtering effort can be drastically reduced while keeping a moderate switching frequency f_{sw} of each half-bridge, which is beneficial in terms of switching losses per device. Note that coupled inductors can be used to symmetrize the individual branch currents i_{Li} and to further reduce the current ripple, while achieving the same or even better transient response [44], [45]. Uncoupled filter inductors, however, are offering the desired flexibility to operate UHBW-PAs either as single-phase high current sources or three-phase lower current sources, which extends

the possible application scenarios as mentioned earlier.

3) Series-Parallel Interleaving:

Since series-interleaving distributes the voltage stress among several devices and parallel interleaved operation distributes the current stress among the parallel branches, a combination of the two approaches gives additional degrees of freedom in terms of loss and stress distribution. For a parallel-interleaved multi-level converter, the effective switching frequency of the current ripple seen by the filter capacitor C is given as

$$f_{sw,eff} = N \cdot (M - 1) \cdot f_{sw} = n_{SC} \cdot f_{sw}, \quad (1)$$

where $n_{SC} = N \cdot (M - 1)$ denotes the total number of utilized SCs. At the same time, the effective (or virtual) switch-node voltage is composed of $n_{SC} + 1$ distinct voltage levels, i.e., the voltage steps applied to the output filter are $\Delta v_{sw,eff} = V_{dc}/n_{SC}$. Considering a required $f_{sw,eff}$ in the range of 5 MHz, a combination of both approaches allows for a low individual device switching frequency f_{sw} and offers both, voltage and current stress sharing.

B. Output Filter Design

To design the single-stage LC output filter, four different constraints are derived based on the general HF equivalent circuit of a switching stage depicted in Fig. 3 (a.i), where $v_{sw,eff}$ denotes the unfiltered $(n_{SC} + 1)$ -level switched

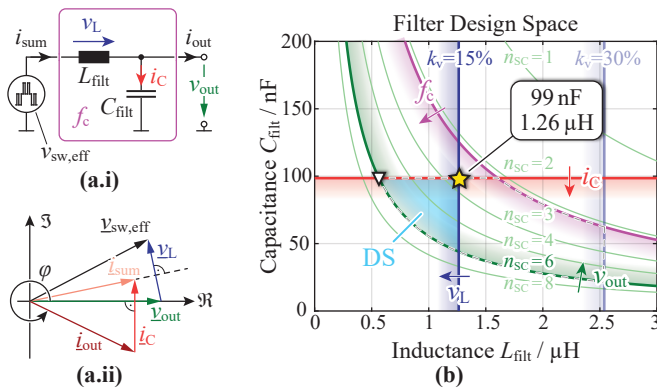


Fig. 3. (a.i) Equivalent circuit of N parallel-interleaved M -level series-interleaved branches indicating the effective switch-node voltage $v_{sw,eff}$, the effective filter inductance L_{filt} and the filter capacitance C_{filt} for a single-stage output filter. (a.ii) Fundamental frequency phasor diagram showing the impact of a load phase angle φ (here: ohmic-inductive load) and the reactive current and voltage in the filter elements. (b) Representation of four design criteria that define the valid range for the filter components in the filter design space according to [46], displayed for different number of switching cells $n_{SC} = N \cdot (M - 1)$. The valid Design Space (DS) for $n_{SC} = 6$ (realizable, e.g., with $M = N = 3$) and the preferred solution highlighted with \star ; Figure based on [10].

voltage with switching frequency $f_{sw,eff}$ that is generated with the series- and parallel-interleaved converter (with arbitrary M and N).

In the resultant filter Design Space (DS) proposed in [46], the criteria are graphically visualized on a L_{filt} vs. C_{filt} plane (cf. **Fig. 3 (b)** for different n_{SC} and highlighted for $n_{SC} = 6$). Note that for the output filter operation it is irrelevant by which combination of M and N a certain n_{SC} is obtained.

The primary goal of UHBW-PA is to achieve maximum BW. This criterion formulated with a minimum ratio k_f between filter corner frequency f_c and maximum output frequency $f_{out,max}$, i.e.,

$$L_{filt} \cdot C_{filt} \leq \frac{1}{(2\pi)^2 \cdot k_f^2 \cdot f_{out,max}^2}, \quad (2)$$

which corresponds to a minimum required f_c to prevent peaking of v_{out} at the maximum output frequency. (2) embodies a hyperbola in the DS and is illustrated with the pink line in **Fig. 3 (b)** for $f_{out,max} = 100$ kHz and $k_f = 4$ (empirical value).

To maximize the output voltage quality (besides the BW the main goal in PAs) a certain maximum peak-to-peak output voltage ripple $\Delta v_{out,pp}$ has to be defined. Assuming a fixed $f_{sw,eff}$, the relative output voltage ripple $\Delta v_{out,pp}/V_{dc}$ is found as

$$\Delta v_{out,pp}/V_{dc} = \frac{1}{32 \cdot n_{SC} \cdot L_{filt} \cdot C_{filt} \cdot f_{sw,eff}^2} \quad (3)$$

and corresponds to a hyperbola in the filter DS (green curves in **Fig. 3 (b)** for different n_{SC} and for $\Delta v_{out,pp}/V_{dc} = 1\%$). There, V_{dc} is the full dc link voltage, even though in practice, a split dc link with $2 \times V_{dc}/2$ is used. With $f_c = 1/(2\pi \cdot \sqrt{L_{filt} C_{filt}})$, (3) can be rearranged to

$$f_c = \sqrt{\frac{8}{\pi^2} \cdot n_{SC} \cdot f_{sw,eff}^2 \cdot \frac{\Delta v_{out,pp}}{V_{dc}}} \quad (4)$$

and shows that with increasing M and/or N (that is, with increasing n_{SC}) the same output voltage quality (e.g., $\Delta v_{out,pp}/V_{dc} = 1\%$) is achieved with a higher filter corner frequency. In fact, (4) gives the maximum allowed f_c to still achieve the desired output voltage quality. This clearly motivates the series- and parallel-interleaved circuit topology, because for a given effective switching frequency $f_{sw,eff} = n_{SC} \cdot f_{sw}$ a realization with series- and parallel-interleaving ($n_{SC} > 1$), thanks to the increased maximum possible f_c , therefore reduces the filtering effort. In any case, a higher f_c allows to use smaller filter components and thereby advantageously helps to minimize the system volume.

Additional design constraints result from the maximum voltage drop v_L and maximum current i_C in the filter elements at the nominal operating point with $V_{out} = 230$ V rms, $P_{out} = 10$ kW (ohmic load) and the maximum output frequency $f_{out,max} = 100$ kHz, i.e., as already calculated in [11],

$$2\pi \cdot f_{out,max} \cdot L_{filt} \cdot I_{out} \leq k_v \cdot V_{out} \quad (5)$$

$$2\pi \cdot f_{out,max} \cdot C_{filt} \cdot V_{out} \leq k_i \cdot I_{out} \quad (6)$$

with the nominal rms output current $I_{out} = P_{out}/V_{out}$ (for an ohmic load). k_v and k_i are the maximum allowed fractions of V_{out} and I_{out} to appear across L_{filt} and flow through C_{filt} , respectively. (5) and (6) correspond to the vertical blue and horizontal red line in the DS in **Fig. 3 (b)** and result in $L_{filt} \leq 1.26$ μ H and $C_{filt} \leq 99$ nF with $k_v = 15\%$ and $k_i = 33\%$. The intersection of the two lines gives the minimum possible f_c . As can be seen with the highlighted valid DS (cyan) for $n_{SC} = 6$, the maximum inductor voltage drop and maximum capacitor current constraints overrule the minimum f_c criterion from (2) for the given values of k_f , k_v and k_i . If, for example, $k_v = 30\%$ would be chosen (semi-transparent blue line), the DS would be limited by the maximum f_c according to (2) for $L_{filt} > 1.6$ μ H (cf. dashed gray outline in **Fig. 3 (b)**). Note that only the output voltage quality criterion depends on n_{SC} . In the interest of maximum output voltage quality, the minimum possible filter corner frequency $f_{c,min} = 1/(2\pi \sqrt{L_{filt,max} C_{filt,max}}) = 472$ kHz (marked with \star in **Fig. 3 (b)**) with $L_{filt,max} = 1.26$ μ H and $C_{filt,max} = 99$ nF is selected. If the smallest possible filter volume is favored, the design with $C_{filt} = C_{filt,max}$ and the minimum required L_{filt} should be selected from the DS (marked with \blacktriangledown in **Fig. 3 (b)** for $n_{SC} = 6$). Generally, a low filter inductance and high filter capacitance facilitates a low converter output impedance to prevent load dependence of the output voltage. Note that depending on the load phase angle φ , the inductive voltage drop across L_{filt} and the capacitive current through C_{filt} lead to an increase or a decrease of $v_{sw,eff}$ and i_{sum} as illustrated with the fundamental frequency phasor diagram in **Fig. 3 (a.ii)**. In the nominal operating point with an ohmic load, the chosen k_v and k_i increase the required $v_{sw,eff}$ by $\approx 1\%$ and i_{sum} by $\approx 4.5\%$.

From **Fig. 3 (b)** follows that a valid DS only results for $n_{SC} \geq 3$, which again proves that for a given $f_{sw,eff}$ a higher n_{SC} is beneficial in terms of filtering, i.e., that for $f_{sw,eff} = 4.8$ MHz, a single 2L ($n_{SC} = 1$) or three-level

($n_{SC} = 2$) SC could not achieve sufficient output voltage quality. As we show later, for the given specifications and the available power semiconductors, only designs with $M \geq 3$ and $N \geq 2$ ($n_{SC} \geq 4$) are feasible.

C. Quantitative Performance Evaluation

To ultimately determine the best-suited combination of N parallel-interleaved M -level series-interleaved branches, a comprehensive simulation model is used to estimate the occurring converter losses. Due to the arbitrary output voltage and current waveform, generally, Hard Switching (HSW) losses occur. Given the at the same time relatively high expected device switching frequency f_{sw} , only GaN power semiconductors can be reasonably utilized in this application, since both, Silicon-Carbide (SiC) and Si devices have too high specific switching losses (either due to the output charge Q_{oss} and/or the reverse recovery charge Q_{rr}). Generally, GaN devices with a small die area and therefore low Q_{oss} are preferred as they have lower Zero-Current Switching (ZCS) and HSW losses. Furthermore, the device must be available in a package that allows adequate heat dissipation, since despite the series- and parallel-interleaved operation, substantial losses per device are expected. To avoid heat dissipation through the Printed Circuit Board (PCB), e.g., by means of thermal vias [48] or advanced PCB technologies such as copper inlays or PCB integrated power devices [49], only top-side cooled devices are considered. Gallium Nitride High-Electron-Mobility Transistors (GaN HEMTs) are available either as High-Voltage (HV) devices with blocking voltage capabilities of 600 – 650 V or as Low-Voltage (LV) devices with blocking voltages of 100 – 200 V. The latter are only applicable for $M \geq 7$ voltage levels and therefore, 600 V devices are better suited for the analysis under the given specifications. 70 m Ω 600 V GaN Gate Injection Transistors (GITs) (a special realization of GaN HEMTs [50]) turned out to be best-suited from the currently available devices on the market in terms of switching performance and particularly regarding heat dissipation capabilities. As will be shown later in more detail, the overall losses are prominently dominated by the HSW losses. This again motivates that in general a low die area and therefore, a low output charge Q_{oss} of the semiconductor is preferred. Moreover, top-side cooled devices allow to decouple the electrical layout of the power commutation loop from the thermal design. Thereby, no thermal vias and/or copper inlays are required, which on the one hand limit the possibilities to design a power commutation loop with as low an inductance as possible and on the other hand would also limit the heat dissipation capabilities because the heat has to flow through the PCB. From the available top-side cooled 600 V/650 V devices, many are intended for high current applications, i.e., feature a low $R_{ds,on}$, thus a relatively large Q_{oss} , and are therefore not well suited for this application. The selected 70 m Ω devices have a Q_{oss} of only 41 nC (at 400 V) and at the same time offer a large metallic cooling pad (area of ≈ 0.8 cm 2). A similar device would be [51] with $R_{ds,on} = 67$ m Ω but it has a higher Q_{oss} of 47 nC (14 % more than [47]) and a smaller cooling pad of only ≈ 0.16 cm 2 (80 % less than [47]). With

estimated losses of ≈ 35 W per semiconductor (cf. **Fig. 4**) the power loss density is the limiting factor for the thermal design and therefore, a large cooling surface is preferred. There are other devices with larger cooling surface, e.g., [52] with ≈ 0.47 cm 2 (still 40 % less compared to [47]) but they have a Q_{oss} of 134 nC ($3 \times$ more compared to [47]), which would significantly increase the already high switching losses (cf. loss breakdown in **Fig. 11**) and are thus not favored. The selected 70 m Ω devices are therefore a reasonable trade-off between the considered aspects. In addition, these particular devices by means of a so-called hybrid drain prevent the phenomenon of increased dynamic on-state resistance (dynamic $R_{ds,on}$) after application of a large drain-source voltage (current collapse) reported to occur in GaN switches [53]. An additional p-GaN region electrically connected to the drain injects holes during the off-state, which completely release the trapped electrons and thus eliminate the effect of the dynamic on-state resistance [54], [55]. This is a significant advantage for operation at high switching frequencies. Therefore, these devices are used for the loss evaluation [47]. It has to be mentioned, however, that there is still a significant temperature dependence of $R_{ds,on}$, which is considered in the loss model by utilizing the worst-case $R_{ds,on}$, i.e., the value at a junction temperature of 125 $^{\circ}$ C.

Fig. 4 shows the result of a detailed loss analysis for different possible converter realizations with N parallel-interleaved M -level series-interleaved branches. **Fig. 4 (a)** shows the conduction losses, **Fig. 4 (b)** the switching losses and **Fig. 4 (c)** the resultant semiconductor efficiency for different combinations of M and N in the nominal operating point. In all cases, the output filter with $L_{filt,max}$ and $C_{filt,max}$ is considered. The reverse conduction losses during the dead time are included in the total conduction losses of **Fig. 4 (a)** assuming a fixed dead time of $t_d = 24$ ns (a more detailed explanation regarding the selection follows just below). Note that at least $M_{min} = 3$ voltage levels are required in each bridge-leg for $V_{dc} = 800$ V when using 600 switches. Similarly, at least $N_{min} = 2$ parallel-interleaved branches are required to not exceed the maximum current rating of the utilized switches (if paralleling of multiple devices is not considered). Moreover, the efficiency target can only be achieved with $N > 2$.

1) Conduction Losses:

From **Fig. 4 (a)**, it can be deduced that for any given N , the conduction losses increase linearly with increasing M , since at any time ($M - 1$) series-connected transistors conduct the branch current. Similarly, for a given M , they scale with $1/N^\alpha$ whereas ideally, $\alpha = 1$, meaning that the current perfectly distributes among the N branches. In practice, $0 < \alpha < 1$ because only the fundamental component of the total inductor current (i_{sum}) splits equally among the N branches but the current ripple does not scale with $1/N$ for a fixed $f_{sw,eff}$ and a fixed L_{filt} . It does, however, reduce with increasing M , because the voltage difference (and hence the voltage-time area) applied to the inductor reduces.

2) Switching Losses:

The switching losses in **Fig. 4 (b)** include calorimetrically measured HSW and Soft Switching (SSW) (Zero Voltage Switching (ZVS)) losses [10]. Depending on the switched

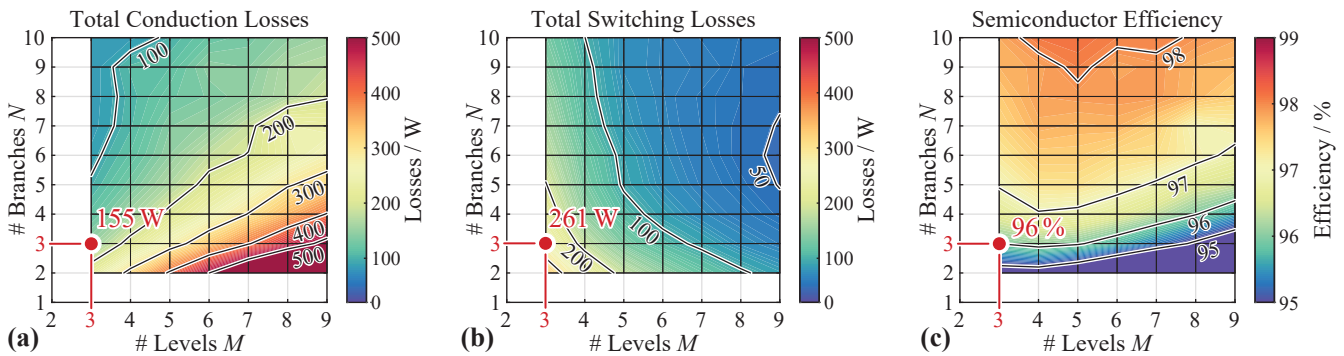


Fig. 4. Characteristics of a class-D amplifier inverter stage realization with N parallel-interleaved M -level Flying Capacitor Converter (FCC) branches. **(a)-(b)** Total power semiconductor conduction and switching losses and **(c)** resulting efficiency considering only the total semiconductor losses. For the calculation, 70 m Ω 600 V Gallium Nitride High-Electron-Mobility Transistors (GaN HEMTs) are considered [47].

current, full ZVS may not be possible within the given dead time ($t_d = 24$ ns in all cases - a minimum t_d is favorable to minimize Low-Frequency (LF) harmonics in v_{out} as will be seen in **Section V-B**), so Partial-Hard Switching (PHSW) occurs where a certain residual charge on the output capacitor is shorted inside the transistor. PHSW losses are modeled based on the approach presented in [56] and are included in the calculation. Note that generally the selection of the dead time is subject to an optimization process to minimize the overall losses. A large dead time enables full ZVS for lower switched currents but at the same time has the disadvantage of increasing the reverse conduction (3rd quadrant) losses due to the increased voltage drop between source and drain. This is in particular a concern with GaN semiconductors, which do not have a physical body diode but are inherently symmetrical devices such that during reverse conduction the voltage between source and drain equals the threshold voltage plus the absolute value of the negative gate to source voltage to keep the transistor safely in the off-state [57]. Ideally, the dead time is adapted based on the switched current in order to always achieve full ZVS without the disadvantage of keeping the complementary device in the off-state for an unnecessary long time with increased reverse conduction losses [56]. A low fixed dead time on the other hand has the advantage of giving the lowest output voltage distortion (cf. **Section V-B**) but achieves full ZVS only for higher switched currents (≈ 4 A in the given case), i.e., PHSW is more likely to occur. In the interest of maximum output voltage quality, a value as low as possible (but fixed) is selected for the dead time ($t_d = 24$ ns) in the following analysis.

The HSW losses per device can be modeled as

$$P_{HSW} = f_{sw} \left(Q_{oss} V_{sw} + \frac{1}{2} \frac{V_{sw}^2}{dv/dt} I_{sw} + \frac{1}{2} \frac{I_{sw}^2}{di/dt} V_{sw} \right) \quad (7)$$

with the transistor output charge Q_{oss} (which is in fact voltage dependent, i.e., $Q_{oss}(V_{sw})$), the switched voltage V_{sw} , the switched current I_{sw} and the voltage and current transition slopes dv/dt and di/dt . Only the effect of charging and discharging of the output capacitor C_{oss} as well as $V-I$ overlap during the turn-on transition (turn-off transition assumed lossless) is considered in (7) [58]. According to [10], the

term in (7) that goes quadratically with I_{sw} can be neglected unless very high currents are switched ($di/dt \rightarrow \infty$). In the considered device, $Q_{oss}(V_{sw})$ scales approximately linearly with V_{sw} and therefore, for a given I_{sw} the HSW losses are expected to scale quadratically with V_{sw} under the simplified assumption of a constant dv/dt independent of the switched voltage and current. For a given V_{sw} , however, a linear relation between the HSW losses and I_{sw} is expected on top of a certain loss offset (ZCS losses, $Q_{oss} V_{sw}$ term). In a series- and parallel-interleaved converter, V_{sw} reduces linearly with M and similarly, the fundamental component of I_{sw} reduces linearly with N . For a fixed $f_{sw,eff}$ and a fixed L_{filt} the current ripple, however, does not scale with N . Therefore, with increasing N (and fixed M), i.e., decreasing fundamental component of I_{sw} but constant current ripple, the HSW losses are expected to scale with $1/N^\beta$ ($\beta > 1$). For low switched currents, that is for high N , the ZCS and/or PHSW and/or SSW losses dominate and the simplified scaling with $1/N^\beta$ is not valid anymore as seen in **Fig. 4 (b)**.

With increasing M (and fixed N) and therefore decreasing V_{sw} a loss scaling with $1/(M-1)^\gamma$ and $\gamma = 2$ would be forecasted using (7). Yet, **Fig. 4 (b)** rather indicates a linear relation, i.e., $\gamma = 1$, which has two reasons:

- i) Calorimetric HSW loss measurements confirm the quadratic dependence on V_{sw} only for low currents ($I_{sw} < 8$ A), but for higher I_{sw} the losses scale linearly with V_{sw} .
- ii) For a given N , the hard switched current I_{sw} increases with increasing M due to the accompanying lower current ripple. This accordingly leads to larger HSW losses and counteracts the expected quadratic decrease.

3) Semiconductor Efficiency:

Finally, **Fig. 4 (c)** shows the resultant expected semiconductor efficiency η_{semi} considering the total forward and reverse conduction, HSW, PHSW and SSW losses, i.e.,

$$\eta_{semi} = \frac{P_{out}}{P_{out} + \underbrace{P_{cond,tot}}_{\text{Fig. 4 (a)}} + \underbrace{P_{sw,tot}}_{\text{Fig. 4 (b)}}} \quad (8)$$

in the nominal operating point ($P_{out} = 10$ kW). As expected from the loss scaling, η_{semi} improves with increasing N ,

whereas for a given N it generally decreases with increasing M as the conduction losses start to dominate. With very high M and N , efficiencies up to 98% are theoretically possible, but come at the expense of a very complex design. Fortunately, the efficiency target is reached already with lower M and N . It has to be kept in mind that the presented calculation only considers one specific switch. For $M \geq 7$, LV 200 V GaN HEMTs could be used, however, as shown in [32], the area-specific on-state resistance $r_{ds,on}^*$ (in $\Omega \cdot \text{m}^2$ or $\text{m}\Omega \cdot \text{mm}^2$) of GaN devices roughly scales linearly with the required Blocking Voltage from Drain to Source (BVDS). Therefore, the penalty of utilizing a high BVDS GaN device at a lower voltage is not as high compared to Si devices, which scale roughly with $\text{BVDS}^{2 \dots 2.5}$.

D. Design Selection

To choose a suitable design, not only the losses but also the volume, particularly of the FCs and the branch inductors, as well as the overall design complexity (e.g. placement of Gate Drivers (GDs) for each of the $2 \cdot n_{\text{SC}}$ switches, layout of the commutation loop in each SC, routing of the signals, etc.) must be considered.

1) Flying Capacitor Volume:

The FC volume is approximated using a polynomial fit of the capacitance density vs. rated voltage from commercially available ceramic capacitors. As shown, e.g., in [40], the required capacitance is found as a function of the peak switched current and the desired *absolute* voltage ripple Δv_{FC} (5 V peak-to-peak in our case) as well as the frequency $f_{iL_{\text{pp}}} = f_{\text{sw,eff}}/N$ at which the FCs are charged and discharged (equal to the current ripple frequency in each branch). The peak switched current reduces slightly with increasing M for a given N thanks to the smaller current ripple and therefore, the required capacitance per FC reduces. By adding an additional voltage level with series-interleaving ($M' = M + 1$), the FC volume automatically increases, since on top of the already present FCs of the M -level series-interleaved bridge leg now an additional FC is placed. While the voltage rating of each additional capacitor is smaller, the overall FC volume still scales linearly with M . However, with increasing N , for a given M , the volume scales even quadratically for three reasons:

- i) Every branch needs the same number of FCs at the same voltage levels (volume scaling linear with N).
- ii) Due to the fixed $f_{\text{sw,eff}}$, $f_{iL_{\text{pp}}}$ reduces with $1/N$. Thus the required capacitance and therefore the required FC volume increases linearly with N .
- iii) The peak switched current, however, does not linearly reduce with increasing N , which would lead to a scaling of the required capacitance and FC volume with $1/N$, but due to the constant current ripple shows a less pronounced dependence on N , as explained earlier.

2) Branch Inductor Volume:

The volume of each individual branch inductor L_{br} scales roughly with $k_{\text{VL}} = L_{\text{br}} \cdot \hat{i}_{L,\text{pk}} \cdot I_{L,\text{rms}}$, where k_{VL} is an indicator for the stored energy in L_{br} . With a fixed value for L_{filt} , the branch inductance scales linearly with N and

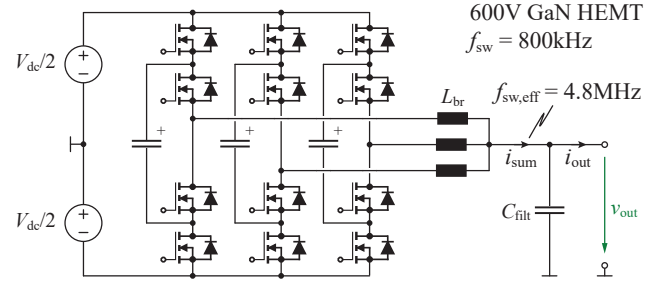


Fig. 5. Topology of the selected three-level triple-interleaved flying capacitor converter (3L3) realized with 70 m Ω 600 V GaN power switches switching at 800 kHz, resulting in an effective switching frequency $f_{\text{sw,eff}}$ of 4.8 MHz.

is independent of M . The branch inductor rms current $I_{L,\text{rms}}$ does not significantly reduce with increasing M (i.e., lower current ripple), but reduces approximately with $1/N$, since it is mainly defined by the fundamental component, which scales with $1/N$. The branch inductor peak current $\hat{i}_{L,\text{pk}}$ slightly reduces with increasing M due to the smaller current ripple and except for high N ($N > 6$) reduces with roughly $1/N$ due to the smaller fundamental component. For $N > 6$, the ripple current dominates and therefore, $\hat{i}_{L,\text{pk}}$ does not reduce any further. All in all, the total volume of all N required branch inductors slightly reduces with increasing M (more pronounced for high N) and increases with increasing N (less pronounced for high M).

3) Three-Level Triple-Interleaved (3L3) Converter:

From the $\eta_{\text{semi}} = 95\%$ contour in **Fig. 4 (c)** can be seen that almost all designs with $N > 2$ (exception $M = 9/N = 3$) are fulfilling the efficiency criterion. It should be noted, however, that additional losses in the converter, e.g., in the inductors, cause the system efficiency η to be smaller than η_{semi} . Therefore, a design with $\eta_{\text{semi}} > 95\%$ has to be chosen. After a comprehensive efficiency, volume and design complexity trade-off, finally the solution with $M = N = 3$, i.e., a Three-Level Triple-Interleaved (3L3) converter topology is selected (highlighted in **Fig. 4**), which is expected to achieve 96% semiconductor efficiency, allows for a very power dense system realization and has manageable design complexity. The topology is depicted in **Fig. 5**. With $n_{\text{SC}} = 6$ switching cells, each transistor has a device switching frequency of $f_{\text{sw}} = 800 \text{ kHz}$ to finally achieve $f_{\text{sw,eff}} = 4.8 \text{ MHz}$ at the summation node. The triple-interleaved design advantageously offers the flexibility to reconfigure the converter for a three-phase output (with $1/3$ power rating in each phase compared to the total single-phase output power) by placing three individual filter capacitors with a capacitance of $C_{\text{filt}}/3$ after each branch inductor. Therefore, the converter can be used, for example, as high BW drive system with sine filter. Please note that a three-level FCC has also been identified in [27] as best-suited for a tracking power supply of a linear RF PA.

III. BRANCH INDUCTOR DESIGN

A. Core Material and Geometry

A vital part of the system are the branch inductors $L_{\text{br}1 \dots 3}$ that give the effective filter inductance $L_{\text{filt}} = 1.26 \mu\text{H}$ (cf. **Fig. 3**). With $N = 3$ branches, each of the three inductors

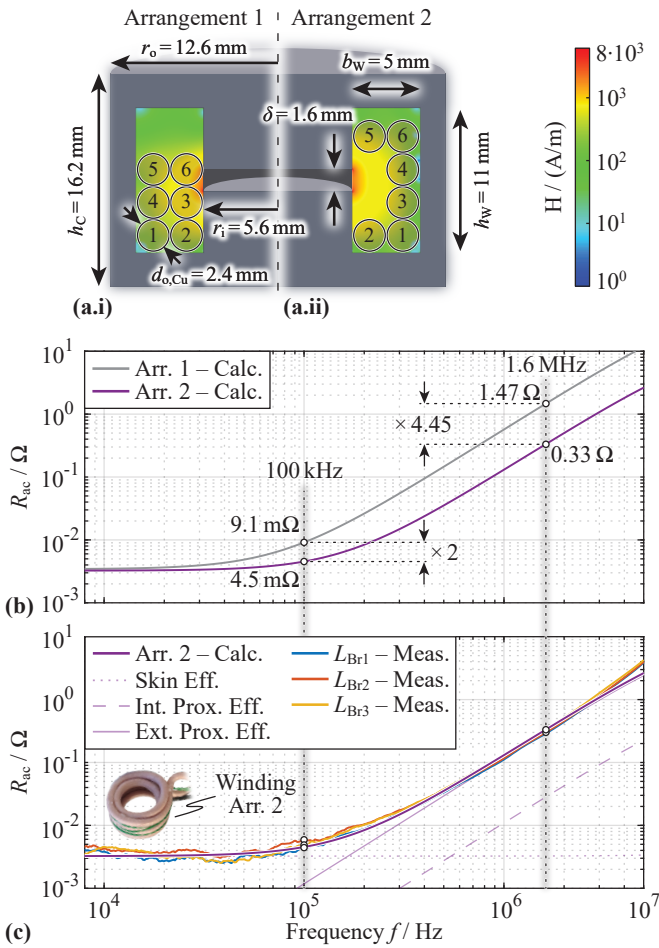


Fig. 6. (a.i) - (a.ii) Comparison of two winding arrangements and the resulting magnetic field H in the winding window assuming an impressed current of 1 A in each turn (obtained with Finite Element Method (FEM) simulations). The dimensions of the utilized pot core are further indicated. **(b)** Calculated ac winding resistance considering the skin effect and the internal and external proximity effect of both investigated winding arrangements. Thereby, the magnetic field determined with FEM simulations is used for the calculation. **(c)** Comparison of the measured inductor ac winding resistance (Arr. 2 - picture of the winding included) with the calculation.

has an inductance of $3.8 \mu\text{H}$ and sees a triangular current ripple with a frequency $f_{iLPP} = f_{sw,eff}/N = 1.6 \text{ MHz}$. Since both, the fundamental and the ripple components of the inductor current are relatively HF, a suitable core material with good HF properties, such as those offered by Manganese-Zinc (MnZn) and Nickel-Zinc (NiZn) ferrites, is required. It should further have a sufficient magnetic permeability μ_T at frequencies in the MHz range without generating excessive core losses. A comprehensive analysis of various available materials has shown that the 3F46 ferrite from Ferroxcube designed for a maximum operating frequency of 1 – 3 MHz is the most suitable.

A pot core geometry that covers the whole winding minimizes the external magnetic stray field around the inductor (magnetic shielding) provided the air gap is only in the center pillar. This is a very important benefit, since it allows to encapsulate the inductor in a metallic housing to facilitate the heat dissipation without generating excessive ac losses due to the proximity effect, as it would be the case for other

core shapes, e.g., E-cores, where the winding heads are not covered by the magnetic material. The required core cross-sectional area A_{Fe} is selected based on the maximum allowed peak magnetic flux density \hat{B} (single-sided amplitude), which necessarily needs to be below the saturation flux density $B_{sat,3F46} \approx 430 \text{ mT} @ 100^\circ\text{C}$, but typically is selected considerably smaller to limit core losses. An empirically determined value $\hat{B} = 250 \text{ mT} < B_{sat,3F46}$ is used in this case. In a simplified assumption, B can be thought of as being composed of two components:

- i) a *current-impressed* fundamental component B_0 and
- ii) a *voltage-impressed* ripple component B_{HF} .

Their respective single-sided amplitudes \hat{B}_0 and \hat{B}_{HF} (peak values) are expressed as

$$\hat{B}_0 = L_{br} \cdot \hat{i}_{L,0} / (N_t \cdot A_{Fe}) \quad (9)$$

$$\hat{B}_{HF} = V_{dc} / (8 \cdot (M - 1) \cdot N_t \cdot f_{iLPP} \cdot A_{Fe}) \quad (10)$$

with the peak fundamental branch inductor current $\hat{i}_{L,0}$ (equal distribution of the sum of the output current i_{out} and the filter capacitor current i_C between the N branches; $\hat{i}_{L,0} = 21 \text{ A}$ in the nominal operating point for $N = 3$) and the number of turns N_t . The worst-case current ripple occurring for duty-cycles $D = 0.5 / (M - 1)$ (and odd multiples thereof) [29] is assumed in (10). The remaining two degrees of freedom are N_t and A_{Fe} , which must be chosen to limit the peak total flux density $\hat{B} \in [\max\{\hat{B}_0, \hat{B}_{HF}\}, \hat{B}_0 + \hat{B}_{HF}]$ accordingly. The worst-case $\hat{B} = \hat{B}_0 + \hat{B}_{HF}$ arises when the maximum current ripple occurs at the same time as the peak fundamental current. Due to the arbitrary load phase angle φ , no a priori statement regarding the location of the worst-case current ripple with respect to the peak fundamental current can be made, hence the worst-case $\hat{B} = \hat{B}_0 + \hat{B}_{HF}$ has to be considered.

Using the well-known area product $A_{Fe}A_w$ (winding window area A_w) [59] a P26/16 core with $A_{Fe} = 87 \text{ mm}^2$ is chosen from all cores of the selected material and shape (core dimensions indicated in **Fig. 6 (a.i)-(a.ii)**). With (9) and (10) together with the now known A_{Fe} , the minimum required number of turns is found as

$$N_{t,min} = \left\lceil \frac{1}{B_{max}A_{Fe}} \left(L_{br}\hat{i}_{L,0} + \frac{V_{dc}}{8(M-1)f_{iLPP}} \right) \right\rceil = 6. \quad (11)$$

This finally results in $\hat{B}_0 = 155 \text{ mT}$ and $\hat{B}_{HF} = 60 \text{ mT}$ and therefore a worst-case $\hat{B} = 215 \text{ mT}$.

B. Winding Arrangement

It was already shown in [10] that HF litz wire results in minimum losses for the given inductor current profile. In particular, the losses at fundamental frequency f_{out} are substantially lower compared to, e.g., solid round or flat wire. The above mentioned encapsulation of the inductor in the metallic housing has the disadvantage that it is more difficult to extract heat from the winding. While heat extraction is improved by potting the winding in the core with a thermally conductive compound (Bergquist TGF 3500LVO), still a relatively conservative maximum LF rms current density

TABLE II. Calculated (italic) and measured (upright) ac resistance at $f = 100$ kHz and $f = 1.6$ MHz with resulting ac winding losses. In all cases, the losses are calculated with the simulated inductor current spectrum at the nominal operating point.

	R_{dc} m Ω	$R_{ac,100k}$ m Ω	$R_{ac,1.6M}$ Ω	P_{100k} W	P_{HF} W	P_{tot} W
Arr. 1	<i>3.40</i>	<i>9.14</i>	<i>1.47</i>	2.10	29.21	31.31
Arr. 2	<i>3.20</i>	<i>4.53</i>	<i>0.33</i>	1.04	6.63	7.67
L_{br1}	3.15	4.41	0.28	1.02	6.59	7.61
L_{br2}	3.46	5.84	0.30	1.28	6.84	8.12
L_{br3}	3.25	4.83	0.33	1.18	7.59	8.77

$S_{rms} = 7$ A is selected to prevent substantial self-heating. With $I_{L,rms} = 17$ A (obtained from circuit simulation at the nominal operating point), a copper cross section $A_{Cu} \approx 2.5$ mm is required. A HF litz wire with 625×71 μ m strands is selected (twisted with $5 \times 5 \times 25$ bundles/strands).

C. AC Winding Losses

The air gap is calculated to obtain the required inductance ($\delta = 1.6$ mm in this case) and as mentioned earlier, is realized only in the center pillar of the pot core to avoid external stray fields. Inside the winding window, however, there is a strong magnetic field near the gap. Consequently, this region must not be filled with turns. **Fig. 6** motivates this by comparing two winding arrangements in the P26/16 core that both lead to the desired L_{br} . In **Fig. 6 (a.i)**, the $N_t = 6$ turns are placed uniformly distributed starting from the bottom (Arrangement 1), whereas in **Fig. 6 (a.ii)** the area in the vicinity of the air gap is kept empty (Arrangement 2). In both cases, the magnetic field H in the winding window is obtained with Finite Element Method (FEM) simulations (also indicated in **Fig. 6 (a.i)-(a.ii)**). Thereby, a homogeneous current density in each turn is assumed (ideal HF litz wire). The ac resistance $R_{ac}(f)$ versus frequency with contributions from the skin effect and proximity effect (internal and external) is then analytically calculated as proposed in [60] using the mean H_{rms}^2 in each of the turns. Of particular interest are the values $R_{ac,100k}$ at $f_{out,max} = 100$ kHz and $R_{ac,1.6M}$ at $f_{iLPP} = 1.6$ MHz. As visualized in **Fig. 6 (b)**, compared to arrangement 1, arrangement 2 reduces $R_{ac,100k}$ by a factor of 2 and $R_{ac,1.6M}$ by almost a factor of 4.5 for the same dc resistance and is therefore clearly preferred.

Finally, **Fig. 6 (c)** compares the measured R_{ac} of the three constructed prototypes according to winding arrangement 2 with the analytically calculated value and reveals very close matching. The measurements are obtained with a precision impedance analyzer (Agilent Technologies 4294A). Moreover, **Fig. 6 (c)** includes a picture of one inductor winding (Arrangement 2) where the empty space on the inner side is visible.

The resulting ac winding losses are estimated with the simulated inductor current spectrum for the nominal operating point and with $R_{ac}(f)$ (calculated and/or measured). **Table II** summarizes the results for the calculated R_{ac} (italic) of arrangements 1 and 2 and the measured R_{ac} (upright) of the three inductors and the resulting ac winding losses. The total losses P_{tot} are split into a fundamental component P_{100k} and a HF component P_{HF} . The latter contains everything except the fundamental component, i.e., all frequency components

above 100 kHz. There are slight variations between the three inductors due to tolerances in the manufacturing, but in general the measured R_{ac} conforms very well with the model. It can be seen that the ac winding losses are mainly determined by the HF components of the current ripple. The calculated R_{ac} in **Fig. 6 (c)** is further decomposed into contributions from the skin-, internal and external proximity effect. The latter clearly dominates R_{ac} for frequencies above several hundred kilohertz and could be reduced by using a litz wire with a smaller strand diameter, e.g., 40 μ m instead of 71 μ m, and more strands to achieve a similar copper cross section area. This would lower P_{HF} (approximately by a factor of 3 – 4 predicted with calculations, i.e., by around 16 – 18 W for all three inductors combined), however, the filling factor is also reduced and the placement of the winding according to arrangement 2 is potentially not possible anymore. In addition, the combined ac winding losses of all three branch inductors are below 25 W, which is a very insignificant part of the total converter losses, as will be shown later.

D. Core Losses and Properties of the Realized Inductors

The realized inductor prototypes are potted in metallic cooling enclosures with the same compound used to pot the winding in the core. The final prototypes have a Self-Resonance Frequency (SRF) of approximately 23 MHz, which is significantly above f_{iLPP} . The saturation current is determined with measurements and exceeds 60 A. The worst-case core losses in the final inductors are roughly estimated with electrical loss measurements with sinusoidal excitation in a series-resonant configuration as proposed in [61]. Due to the highly non-uniform flux distribution in pot cores, the P26/16 core is also used for the loss measurements in order to have conditions as similar as possible to those in the final operation. Pure ac excitation with 100 kHz and $\hat{B}_0 = 155$ mT results in losses of ≈ 1.1 W. Similarly, a HF excitation with a sinusoidal flux density profile with $f_{iLPP} = 1.6$ MHz and $\hat{B}_{HF,\sim} = 49$ mT (amplitude of the first harmonic in the triangular flux density profile with $\hat{B}_{HF} = 60$ mT, cf. (10)) on top of a dc bias $B_{dc} = [0, 77, 100, 125, 155]$ mT results in losses of [1.53, 2.45, 3.01, 4.17, 4.34] W. Therefore, the worst-case weighted core losses over one fundamental period are ≈ 4.2 W (sum of the 100 kHz loss component and the weighted HF ripple components for different dc bias flux densities occurring over one fundamental period). Here, always the maximum HF flux density ripple is assumed. In practice, depending on the duty-cycle, the HF flux density ripple and therefore the associated core losses are smaller, so core losses of ≈ 4.2 W per inductor are a worst-case approximation. Due to the large surface and very good thermal connection of the core to the cooling housing, the core losses can anyway be dissipated very well. Furthermore, similar to the ac winding losses, compared to the semiconductor losses, the core losses do not significantly influence the system efficiency.

IV. HARDWARE DEMONSTRATOR

This section describes the development of a 3L3 converter hardware prototype, which is used to demonstrate the full func-

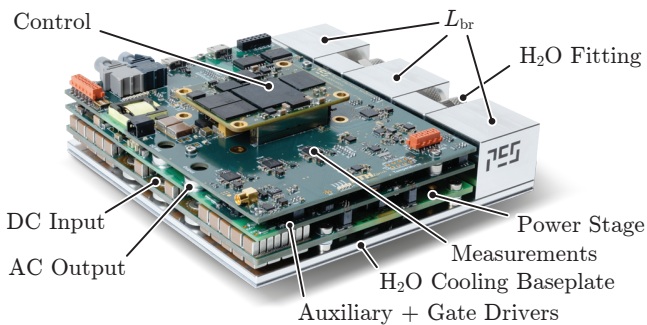


Fig. 7. Picture of the realized hardware demonstrator of the single-phase 10kVA power amplifier with the most important building blocks labeled. The overall dimensions of $123\text{ mm} \times 123\text{ mm} \times 26.5\text{ mm}$ give a power density of 25 kW/dm^3 (410 W/in^3).

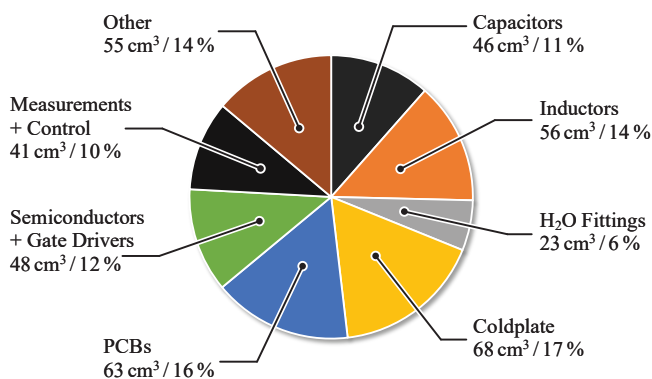


Fig. 8. Volume breakdown of the hardware demonstrator indicating the absolute and relative contribution of the individual building blocks/components.

tionality of the system, i.e., operation at the high $f_{\text{sw,eff}}$ and the high output voltage quality, and to verify the predicted system efficiency. **Fig. 7** shows a picture of the realized prototype and highlights the very compact realization (overall dimensions of $123\text{ mm} \times 123\text{ mm} \times 26.5\text{ mm}$, Field-Programmable Gate Array (FPGA) board not included, since this could be soldered directly on the top PCB) with a boxed volume of only 400 cm^3 (24.4 in^3), which results in a power density of 25 kW/dm^3 (410 W/in^3). The most relevant system building blocks and the dc input/ac output interfaces are labeled. The converter consists of three PCBs, starting with the power section (power transistors, GDs, dc link and flying capacitors) at the bottom, the GD supply, the HV auxiliary supply and part of the measurement circuits in the middle and at the top the Analog-to-Digital Converters (ADCs) and the FPGA to control the system. Furthermore, the top PCB features several communication interfaces to connect the converter with a host computer. The whole system is mounted on a custom manufactured coldplate as part of a liquid cooling system (cf. **Section IV-B**). The cubes in the background contain the three branch inductors L_{br} (cf. **Section III**) and the connection (fittings) for the liquid cooling system.

The volume breakdown of the 3L3 converter shown in **Fig. 8** indicates a very uniform distribution between the different components. Remarkable is that the PCBs, the fittings for the liquid cooling system and the coldplate already account

for almost 40% of the total volume. The capacitor share is composed of the dc link capacitors ($\approx 14\text{ }\mu\text{F}$ effective capacitance between DC+ and DC- at $V_{\text{dc}} = 800\text{ V}$, split as $2 \times 28\text{ }\mu\text{F}$ at 400 V at the split dc link), the FCs ($\approx 6\text{ }\mu\text{F}$ effective capacitance at $V_{\text{FC}} = 400\text{ V}$) and the output filter capacitance ($3 \times 33\text{ nF C0G}$).

A. Power Stage Layout Considerations

To minimize the $V - I$ overlap losses, the switching transitions must be as fast as possible (high dv/dt , cf. (7)), demanding careful layout of the GDs and the power commutation loop. **Fig. 9 (a)** shows the bottom view of the power stage PCB with the top-side cooled switches. The layout of the three branches is fully modular and could easily be extended for any N . **Fig. 9 (b)** exemplary highlights the coplanar commutation loop layout for the outer switching cell of the third branch ($T_{8\text{H}3}$ and $T_{8\text{L}3}$). The layout is identical for all six switching cells. The copper plane on the inner layer 6 (distance of $150\text{ }\mu\text{m}$ to the bottom layer where the switches are mounted, cf. **Fig. 9 (d)**) is on "DC-" potential and provides a coplanar return path for the commutation current (indicated with the blue and cyan arrow for current flow on the bottom and the inner layer 6, respectively). Measurements reveal a contribution of the PCB layout to the power loop inductance of $< 2.2\text{ nH}$ for the outer switching cells and of $< 1.5\text{ nH}$ for the inner switching cells (copper plates that cover the entire semiconductor footprint are used instead of the transistors to account solely the PCB contribution). In the latter case, the inductance is lower because the source of $T_{4\text{H}i}$ and the drain of $T_{4\text{L}i}$ are directly connected at the respective switch-nodes "SW i " ($i \in \{1, 2, 3\}$). Related to the device internal inductance of 3.5 nH between drain and source, the layout does not significantly contribute to the overall power loop inductance.

Fig. 9 (c) shows the GD layout of $T_{4\text{L}3}$ (identical layout for all 12 switches). In contrast to Metal-Oxide-Semiconductor Field-Effect Transistors (MOSFETs) with an isolated gate, the utilized GaN GITs have a diode between gate and source, which after turn-on requires a small steady-state gate current $I_{\text{g,ss}}$ to flow [57]. Therefore, a GD circuit featuring an ac-coupled high current turn-on path and in parallel a dc-coupled path for the small $I_{\text{g,ss}}$ based on the one proposed in [62] is utilized. In this case, the GD has a bipolar supply to ensure a constant negative bias $V_{\text{GD-}} = -5\text{ V}$ in the off-state to prevent parasitic turn-on. Similar to the power loop, the gate loop is realized coplanar to minimize the loop inductance (return path on inner layer 1). Measurements reveal a turn-on and turn-off gate loop inductance of $L_{\text{g,on}} \approx 3\text{ nH}$ and $L_{\text{g,off}} \approx 4\text{ nH}$. Since the GD Integrated Circuit (IC) sink pin (for the turn-off) is located further away from the GaN transistor, it makes sense that $L_{\text{g,off}} > L_{\text{g,on}}$. Compared to the measured device internal gate to source loop inductance of $L_{\text{G,int}} \approx 7\text{ nH}$, the external contribution is minor. Strict care was taken to prevent overlapping copper of jumping potentials (e.g. the source nodes) and logic nets (e.g. PWM, enable or measurement signals coming from/going to the FPGA), which would introduce significant CM current over the parasitic

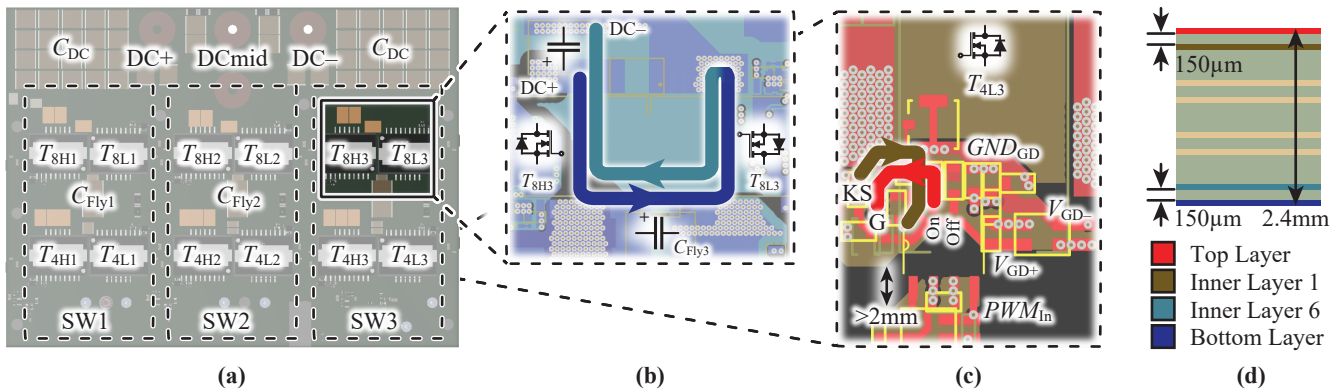


Fig. 9. (a) Power stage of the 3L3 with highlighted individual branches and corresponding components. (b) Detailed view of the coplanar power commutation loop (drain to source) in the outer FC cell of branch 3. (c) Detailed view of the coplanar Gate (G) to Kelvin Source (KS; equal to GND_{GD} potential) commutation loop of one switch (T_{4L3}) (turn-on path highlighted; equivalent for the turn-off path). (d) Layer stack of the 2.4 mm thick power PCB. Each copper layer has a thickness of 70 μm (2 oz.).

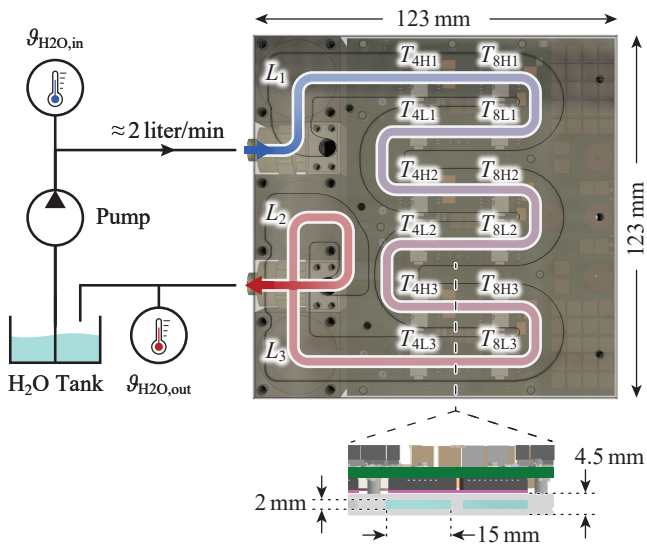


Fig. 10. Simplified setup of the liquid cooling solution for the 3L3 converter with indicated dimensions of the overall system (123 \times 123 mm), the thickness of the coldplate (4.5 mm) and the dimensions of the liquid cooling channel (15 \times 2 mm). From the measured coolant inlet and outlet temperature and the volume flow of approximately 2l/min, the total losses can be estimated.

capacitance due to the high dv/dt and potentially lead to distortions and/or malfunction of the digital circuit.

B. Cooling System

An anticipated semiconductor efficiency of $\eta_{\text{semi}} = 96\%$ at a power level of $P_{\text{out}} = 10\text{ kW}$ (nominal ohmic load) results in power losses of roughly $P_{\text{loss,device}} = 35\text{ W}$ in each switching transistor of the 3L3 design (total semiconductor losses $\approx 420\text{ W}$). The resultant semiconductor power loss density of $\approx 42\text{ W/cm}^2$ demands for liquid cooling to efficiently dissipate the heat without excessive temperature rise [63]. Along with reliability concerns, a too high junction temperature ϑ_j of the GaN transistor substantially increases the conduction losses because of the very pronounced temperature dependence of the on-state resistance $R_{\text{ds,on}}$ [53]. A custom-milled aluminum liquid cooling coldplate to cool the 12 power transistors and

the three branch inductors is designed. **Fig. 10** shows a semi-transparent bottom view of the coldplate and the power PCB. The path for the coolant (H_2O in this case) from the inlet (cold side, blue) to the output (hot side, red) through the single meandering channel as well as the positions of the components to be cooled are highlighted. A detailed side view of the assembly is shown at the bottom of **Fig. 10**. The rectangular water channel is 15 mm wide to match the width of the power transistor's heat pad. Due to the coldplate's low profile of only 3 mm (2 mm channel height), the 1.5 mm thick cover plate is glued to the coldplate to ensure a fully sealed assembly. An electrically insulating thermal gap pad (indicated with pink color) attaches the transistors to the coldplate.

With the resulting volume flow of roughly $\dot{V} = 2\text{ l/min}$ and the measured water inlet and outlet temperatures $\vartheta_{\text{H}_2\text{O,in}}$ and $\vartheta_{\text{H}_2\text{O,out}}$, the losses can be estimated from the basic heat transfer equation with

$$P_{\text{loss,tot}} \approx \dot{Q} = \rho_{\text{H}_2\text{O}} \cdot \dot{V} \cdot c_{\text{H}_2\text{O}} \cdot (\vartheta_{\text{H}_2\text{O,out}} - \vartheta_{\text{H}_2\text{O,in}}) \quad (12)$$

where $c_{\text{H}_2\text{O}} = 4181\text{ J/(kg}\cdot\text{K)}$ is the specific heat capacity and $\rho_{\text{H}_2\text{O}} = 997\text{ kg/m}^3$ the density of water at a temperature of 25°C, respectively. Note that (12) neglects heat dissipation from the surface of the coldplate, e.g., through natural convection or radiation. Therefore, the actual total losses are slightly higher than the estimated ones. With (12), the calculated total losses of $\approx 420\text{ W}$ would only lead to a temperature difference of 3 K, which is difficult to measure accurately. Nevertheless, the simple estimation is a good sanity check for the precision electrical loss measurements presented later (cf. **Section V-A**). Note that the coolant (H_2O) heats up while flowing from the inlet towards the outlet such that, e.g., underneath T_{8L3} and T_{4L3} the temperature is already higher than the inlet temperature $\vartheta_{\text{H}_2\text{O,in}}$. This could in principle lead to unequal semiconductor temperatures and therefore, to unbalanced losses (e.g., due to the strongly temperature-dependent on-state resistance in GaN devices). However, thanks to the relatively high volume flow and short channel length, with the given cooling solution the overall temperature difference between inlet and outlet is only roughly 3 K (at maximum losses of $\approx 420\text{ W}$) and therefore, there is

TABLE III. Available measurements on the 3L3 converter with their sampling rate f_s , resolution B and Bandwidth (BW).

Signal	f_s	B	BW
Output Voltage v_{out}	125 MSPS	14 Bit	≈ 30 MHz
Load Voltage v_{load}	125 MSPS	14 Bit	≈ 30 MHz
Output Current i_{out}	125 MSPS	14 Bit	> 30 MHz
Summed Ind. Current i_{sum}	125 MSPS	14 Bit	> 30 MHz
Branch Currents $i_{Lbr1...3}$	3.125 MSPS	14 Bit	≈ 1 MHz
FC Voltages $v_{FC1...3}$	3.125 MSPS	14 Bit	≈ 100 kHz
DC Link Voltages v_{dcp}, v_{dcn}	3.125 MSPS	14 Bit	≈ 800 kHz

no significant uneven temperature distribution that could have an influence on the loss sharing and the symmetric current handling, as verified in **Fig. 15**. There are alternative cooling channel geometries, which do ensure a more symmetrical temperature distribution, i.e., multiple parallel channels, which is of particular importance for large heat sinks. There, it must be ensured that the volume flow is equal in all parallel channels as otherwise the temperature distribution can be significantly non-uniform [63]. The geometry in **Fig. 10** is mainly selected because it inherently ensures equal volume flow throughout the channel, allows for a straight-forward channel design and still gives a small overall temperature difference thanks to the relatively small dimensions and the high volume flow.

C. Measurement Circuits and Control

An FPGA is responsible for the PWM pattern generation, the processing of measurement signals, the supervision of voltages and currents and for the communication with a host computer. In this article, the 3L3 is operated without closed-loop control but in a next step, suitable control schemes such as the ones proposed in [64] are implemented. This has to be done directly in hardware on the FPGA for maximum controller update rate, i.e., to minimize execution time. As shown in [64], a crucial part to achieve a high control BW is to minimize the overall loop delay, which includes the measurements (latency of the ADC), the execution time inside the FPGA (pipeline latency) and the signal isolator and GD delays. An ADC with a sampling rate of 125 MHz and a latency of 5 clock cycles (Analog Devices LTC2255) is used to sample the summed inductor current i_{sum} , the output voltage v_{out} and the output current i_{out} . The transistors are driven with an isolated GD IC featuring a low propagation delay and a very tightly specified jitter (Silicon Labs/Skyworks Si8271). Apart from a small loop delay, very high BW voltage and current measurements are required. The latter have been extensively analyzed in [65], [66] and finally, an off-the-shelf Hall-effect current sensor extended with a current transformer to achieve a BW > 30 MHz is integrated into the 3L3. **Table III** summarizes all available measurements with their sampling rate and resolution that can be performed with the converter. Note that the v_{load} measurement can be used for ac load sensing to compensate, e.g., the voltage drop across the inductance connecting the output of the 3L3 with the load or to impress a certain output impedance as shown in [6].

All measurements from **Table III** are additionally used for overvoltage and overcurrent protection with ultra-fast response, i.e., within few tens of nanoseconds.

V. PERFORMANCE VERIFICATION

This section presents experimental measurement results to verify the performance of the 3L3 hardware prototype. As mentioned above, the converter is operated in open-loop configuration.

A. Efficiency and Losses

The system efficiency η is electrically measured for sinusoidal output voltages with a constant rms value $V_{out} = 230$ V at different output power levels $P_{out} \in \{3.3 \text{ kW}, 5 \text{ kW}, 7.3 \text{ kW}, 8 \text{ kW}, 9 \text{ kW}, 10 \text{ kW}\}$ (purely ohmic load) and for different output frequencies $f_{out} \in \{10 \text{ kHz}, 20 \text{ kHz}, 50 \text{ kHz}, 100 \text{ kHz}\}$.

In all cases, the system is supplied with a split dc link composed of two 400 V dc voltage sources and a fixed dead time $t_d = 24$ ns is set. The load resistor R_L is realized with multiple parallel low-inductive planar resistors (Ohmite TAP800). To minimize the parasitic inductance L_L from the connection between converter output and load, depending on P_{out} , multiple separate load resistor assemblies are connected directly to the converter output. At maximum f_{out} and P_{out} , the influence of L_L is the strongest, since at this operating point simultaneously the inductive voltage drop becomes maximum and the load resistance minimum. This worst-case corresponds to the nominal operating point, where $L_L \approx 1.4 \mu\text{H}$, and results in a phase-shift of roughly 10° between v_{out} and i_{out} ($\cos(\varphi) = 0.985$). **Appendix A** derives the maximum possible output power for different load phase angles φ . An output power derating of maximum 27.5 % is required for purely capacitive loads.

The efficiency measurements are performed with a precision power analyzer (Yokogawa WT3000) and are depicted in **Fig. 11 (a)**. The measured efficiency (dots) is compared with calculations (continuous lines) resulting from the loss model introduced in **Section II-C**, additionally including the branch inductor ac winding losses according to **Section III-C**. The target efficiency of 95 % is achieved over a very wide range of P_{out} and f_{out} . In the nominal operating point (marked with \star) the efficiency is 95.8 %. The partial load efficiency is worse for higher f_{out} because of the capacitive current i_c in C_{filt} , which depends solely on f_{out} and v_{out} and not on P_{out} (for a fixed output voltage). This current generates switching and conduction losses in the power stage. Furthermore, **Fig. 11** shows detailed calculated loss breakdowns for **(b)** $f_{out} = 10$ kHz, **(c)** $f_{out} = 50$ kHz and **(d)** $f_{out} = 100$ kHz. In general, the measurements conform very well with the calculations and the absolute difference between the measured and calculated losses is < 25 W. Because measurements give a better efficiency at low P_{out} than the calculations but a lower efficiency at high P_{out} , it can be concluded that the model underestimates ohmic losses and slightly overestimates constant losses (independent of P_{out}) and/or losses scaling linear with P_{out} . More specifically, since the effect is more pronounced for high f_{out} , the real system has more ac resistance in the power path than modeled. Potential sources for the ac resistance are, e.g., the primary conductor of the current transformers (two in total), PCB tracks carrying the

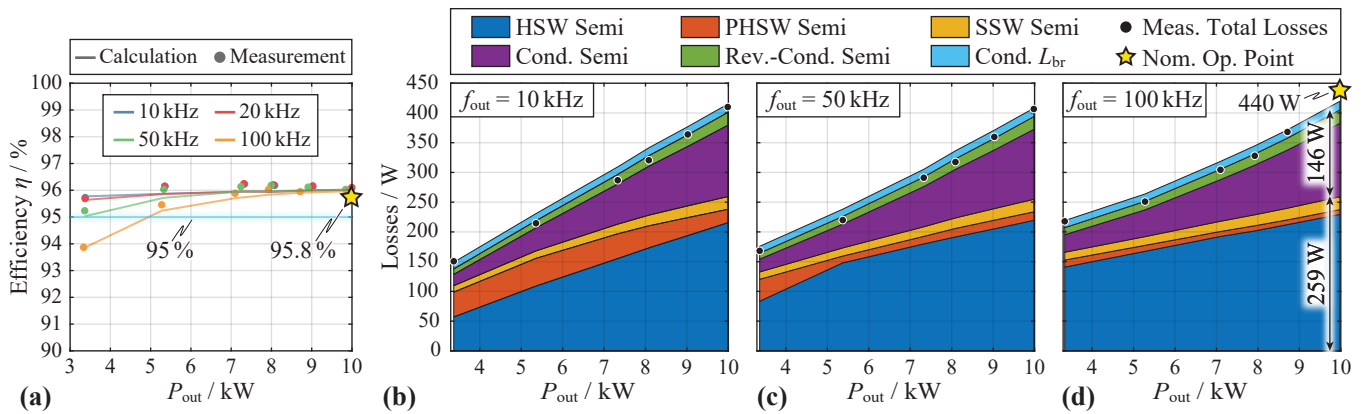


Fig. 11. (a) Measured (dots) and calculated (lines) system efficiency for different output frequencies (10 kHz - blue, 20 kHz - red, 50 kHz - green and 100 kHz - orange) vs. output power P_{out} with an ohmic load, an output rms voltage of $V_{out} = 230$ V and a fixed dead time (interlocking delay) of $t_d = 24$ ns. (b) - (d) Calculated loss breakdown indicating hard switching (HSW, blue), partial-hard switching (PHSW, orange), soft switching (SSW, yellow) losses, semiconductor conduction losses (purple), semiconductor reverse conduction losses (green) and inductor conduction losses (cyan) for an output frequency of (b) 10 kHz, (c) 50 kHz and (d) 100 kHz. Further included are the measured total losses (black dots) in comparison with the loss model. The nominal operating point (10 kW ohmic/100 kHz) is marked with \star .

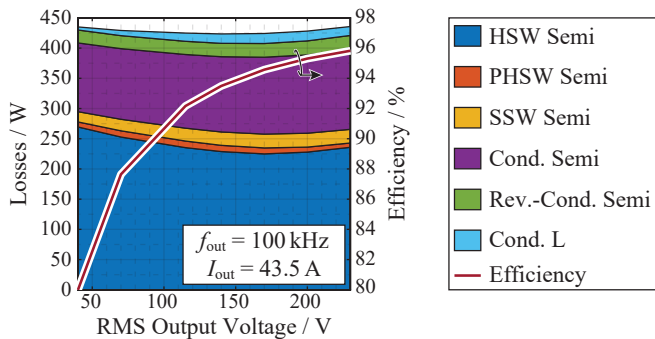


Fig. 12. Calculated efficiency and loss breakdown for operation with $f_{out} = 100$ kHz at maximum rms output current $I_{out} = P_{out,max}/V_{out,nom} = 43.5$ A and varying rms output voltage V_{out} into a purely ohmic load.

load current (in particular the return connection from the summing node to the filter capacitor located next to the dc link) and contact resistance of soldering joints. **Fig. 11 (d)** nicely shows the loss “offset” for $f_{out} = 100$ kHz compared to $f_{out} = 10$ kHz, even at low P_{out} , due to the higher switching losses given by the aforementioned capacitive current in C_{filt} . The semiconductor loss distribution in the nominal operating point (marked with \star) is practically identical to the one in **Fig. 4** for the $M = N = 3$ design.

Furthermore, **Fig. 11 (b)** and (c) reveal that for $f_{out} = 10$ kHz and 50 kHz a better partial load efficiency (lower losses) could be achieved by implementing an adaptive dead time, which enables full ZVS also for lower switched currents. Since this would require an increase of t_d from its minimum value of 24 ns and in turn would lead to a distortion of the output voltage, further measures would need to be implemented to compensate this effect (cf. **Section V-B**).

Fig. 12 depicts the efficiency and a breakdown of the calculated losses (obtained with the extended loss model also used in **Fig. 11**) for operation with $f_{out} = 100$ kHz and full-scale output current, i.e., an rms output current $I_{out} = P_{out,max}/V_{out,nom} = 43.5$ A into a purely ohmic

load, for different rms output voltages V_{out} between 40 V and 230 V (nominal operating point). This corresponds to the worst-case operating mode, since the output power decreases linearly with output voltage and the output current is always maximum. The efficiency drops from 96% in the nominal operating point ($V_{out} = 230$ V and $P_{out} = 10$ kW) to 80% for $V_{out} = 40$ V and $P_{out} = 1.74$ kW. This is expected, since the total losses do not reduce with lower output voltage (they are more or less constant and show a slight bathtub shape), whereas the output power does (linear decrease with decreasing V_{out}). The bathtub shape of the losses can be explained with the current ripple, which depends on the modulation depth (and therefore on V_{out}). Reducing the output voltage from the nominal value of 230 V initially increases the current ripple (duty-cycle more often close to 0.25 and 0.75, which gives maximum current ripple in a three-level FCC [26]) and therefore, leads to reduced HSW losses (lower current switched hard) and more PHSW and SSW transitions. With further output voltage reduction (below approximately 170 V rms), the ripple is reduced because the duty-cycle is always close to 0.5, which in a three-level FCC gives minimum current ripple [26]. Opposite to the case of large ripple, this leads to more HSW losses (higher current switched hard) and less PHSW and SSW transitions. The conduction losses, however, slightly decrease thanks to the lower ripple but this decrease has negligible impact on the total losses. The reduced current ripple also explains the lower inductor conduction losses for low output voltages, which according to **Table II** are predominated by the HF losses (current ripple) at $f_{iL,pp}$ due to the substantially higher ac resistance at $f_{iL,pp}$ compared to f_{out} (approximately a factor of 50). Despite the efficiency degradation with reduced output voltage in this worst-case operation mode it is still substantially higher compared to linear PAs (best-case efficiency of 78.5% for a full-scale output into a purely ohmic load [11]).

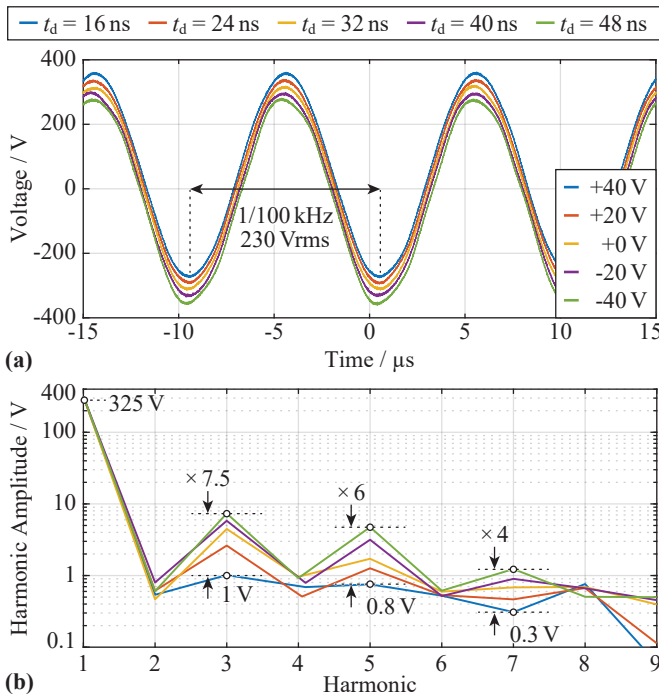


Fig. 13. Influence of the dead time t_d on the output voltage quality with a quasi-analog PWM modulator (125 MHz update rate). (a) Measured output voltage ($f_{\text{out}} = 100 \text{ kHz}$, $V_{\text{out}} = 230 \text{ V rms}$, $P_{\text{out}} = 3.3 \text{ kW}$, ohmic load). The measurements are offset by multiples of 20 V to visualize the differences in the waveforms. (b) Corresponding output voltage amplitude spectra with the 9 lowest harmonics of f_{out} .

B. Output Voltage Quality

Phase-Shifted PWM (PSPWM), where one reference signal v_{ref} is compared with n_{SC} phase-shifted carrier signals, each with a frequency f_{sw} (device switching frequency) is one possible modulation strategy for series- and/or parallel-interleaved converters [67]. This strategy is used in the presented 3L3 converter. Digital implementation of the PWM offers maximum flexibility, but has the disadvantage of finite horizontal (time) and vertical (amplitude) resolution. It was shown in [64] that a regularly sampled PWM (also called synchronous PWM), where the compare values/duty-cycles are updated at the top and bottom of a triangular carrier signal introduces a time delay T_d of $3/(2f_{\text{sw,eff}}) = 312.5 \text{ ns}$ (with $f_{\text{sw,eff}} = 4.8 \text{ MHz}$), which can substantially limit the maximum achievable controller BW. Therefore, a quasi-continuous operation of the PWM unit is favorable, i.e., the duty-cycles are updated in every FPGA clock period, resulting in an update rate of $f_{\text{PWM}} = f_{\text{clk}} = 125 \text{ MHz}$, where 125 MHz is the maximum achievable FPGA clock frequency. This implementation is comparable to a naturally sampling PWM [30] and is used in the 3L3 to virtually eliminate the PWM delay [68]. The vertical resolution is limited by the ratio of FPGA clock frequency to the symmetric (triangular) carrier signal frequency f_{sw} . The number of possible duty-cycles equals $\lfloor f_{\text{clk}}/(2 \cdot f_{\text{sw}}) \rfloor = 78$. The 3L3 can set the local average of the switch-node voltage $\langle v_{\text{sw}} \rangle$ (mean over one switching period) with a resolution of $\Delta \langle v_{\text{sw}} \rangle = V_{\text{dc}}/78 = 10.25 \text{ V}$ in each branch. Effectively, this corresponds to a voltage resolution $\Delta \langle v_{\text{sw,eff}} \rangle = \Delta v_{\text{sw}}/N = 3.42 \text{ V}$ (local average of

the effective switch-node voltage $v_{\text{sw,eff}}$) thanks to the parallel-interleaved topology. A further reduction of $\Delta \langle v_{\text{sw,eff}} \rangle$ would be possible with a High-Resolution PWM (HRPWM), which is currently being investigated as part of ongoing research on this topic.

Fig. 13 (a) shows measured output voltages at $f_{\text{out}} = 100 \text{ kHz}$, $V_{\text{out}} = 230 \text{ V rms}$ and $P_{\text{out}} = 3.3 \text{ kW}$ (ohmic load) for different dead times t_d (interlocking delays). Note that the different waveforms are offset by multiples of 20 V to better visualize the distortions. The resulting output voltage spectra are depicted in **Fig. 13 (b)** and indicate the presence of odd harmonics of the output voltage. With a higher t_d , the amplitudes of the odd harmonics are increasing, which is also visible in **Fig. 13 (a)** as distorted waveform around the minima and maxima of the sine. Compared to $t_d = 48 \text{ ns}$, for $t_d = 16 \text{ ns}$, the 3rd and 5th harmonic are substantially reduced from 7.5 V to 1 V and from 4.8 V to 0.8 V, respectively. During the dead time, depending on the direction of the switched current, either a resonant ZVS transition starts, which directly after the turn-off signal from the FPGA changes the switch-node voltage (SSW), or the switch to be turned off goes into reverse conduction and only after the signal to turn on the complementary switch, i.e., after t_d , the switch-node voltage changes (HSW). This is a fundamental cause of non-linearities, in particular the source of odd harmonics [69], because depending on the direction and magnitude of the switched current, a voltage-time area is applied to the inductor, which is different from the one calculated in the controller [70]. Nevertheless, **Fig. 13** indicates a very high output voltage quality for low t_d . A further improvement, however, could be desired, e.g., to reduce the error voltage applied to the output voltage controller. A common strategy to mitigate the dead time nonlinearities is to delay the switching pulses in the FPGA depending on the current direction and magnitude to effectively apply the correct voltage-time area to the inductor. This acts as feed-forward term to correct the dead time induced non-linearities. Alternatively, the actual pulses at the switch-node can be measured and compared with the ideal PWM pulses (without the dead time), which does not need output current sign and/or magnitude measurements. Noise-shaping is then applied to shift the dead time induced non-linearities to higher frequencies [71]. While the accurate measurement of the fast pulses at the switch-node can be difficult because of HF noise coming from the extremely fast dv/dt in GaN transistors, the noise-shaping approach further requires that f_{sw} (and not $f_{\text{sw,eff}}$ because the dead time is present for every SC, i.e., occurs in every switching period $1/f_{\text{sw}}$) is significantly greater than f_{out} (typically, $f_{\text{sw}}/f_{\text{out}} > 10$ [71]), which is not given in our application. In the current implementation, no dead time correction is used and therefore, a minimum t_d should be selected in the interest of maximum output voltage quality. Because efficiency measurements showed that $t_d = 24 \text{ ns}$ has the lowest losses, this value is finally selected. The amplitudes of the 3rd and 5th harmonic are 2.5 V and 1.2 V, respectively in this case, which is still lower than $\Delta \langle v_{\text{sw,eff}} \rangle$.

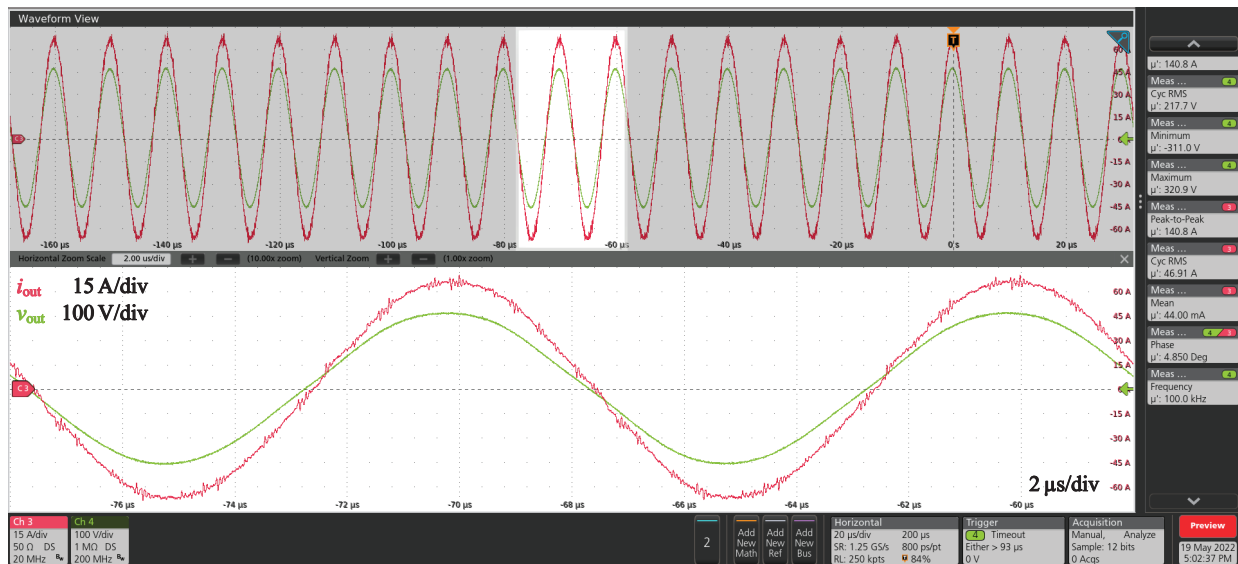


Fig. 14. Measured waveforms of the output voltage (green, 100 V/div) and output current (red, 15 A/div) of a 100 kHz fundamental frequency large-signal (230 V_{rms}) sine and an output power P_{out} of 10 kW (ohmic load). Time scale of the zoomed view is 2 μ s/div.

C. Exemplary Waveforms at Nominal Operating Point

Fig. 14 shows the measured output voltage v_{out} (green; 100 V/div) and output current i_{out} (red; 15 A/div) in the nominal operating point ($f_{out} = 100$ kHz, $P_{out} = 10$ kW (ohmic load), $V_{out} = 230$ V rms). The output represents a clean sine wave without harmonic distortion. In **Fig. 15**, the measured individual branch inductor currents i_{L1} (blue; 6 A/div), i_{L2} (red; 6 A/div) and i_{L3} (green; 6 A/div) and the calculated summed current i_{sum} (orange; 18 A/div) are depicted for the same operating point. It can be seen that the three currents are symmetrically distributed and correctly phase-shifted by 120° between the branches. The ripple on the resulting summed current i_{sum} is therefore significantly limited (note the different vertical scale in **Fig. 15**). At the moment, no active (closed-loop) current balancing is employed, i.e., the current sharing is established purely by the application of the same reference signal to the PWM modulator in each branch (nominally identical voltage-time areas applied to each L_{br}) and by the parasitic resistances ($R_{ds,on}$ of the transistors and the winding resistance of L_{br}). The FC voltages are naturally balanced with an error $< \pm 2\%$ of the nominal voltage thanks to the inherent losses in the power stage. Active balancing would be possible with the currently implemented modulation to further improve the steady-state FC balancing but is not used at this stage.

Due to the compact realization and the mounting of the top-side cooled switches on the coldplate, the temperature distribution of the switches could not be measured during operation, e.g., with a thermal camera. The switch case temperatures as well as the branch inductor winding temperatures are measured with Negative Temperature Coefficient (NTC) temperature sensors. For a H_2O inlet temperature of $\vartheta_{H_2O,in} = 30^\circ C$ the semiconductor case temperatures are all below $60^\circ C$. With a datasheet specified thermal resistance from junction to case of $R_{th,j-c} = 1$ K/W and with approximately 35 W losses per switch this leads to a junction temperature $\vartheta_j \approx 95^\circ C$,

which is well below the maximum allowed value. The inductor winding temperatures are all below 40° .

VI. CONCLUSION

The growing prevalence of power electronic converter systems featuring Wide-Bandgap (WBG) semiconductors with ever higher switching frequencies motivate the need for Ultra-High Bandwidth Power Amplifiers (UHBW-PAs) for characterization and testing purposes. In this article, circuit topologies for a switch-mode (Class-D) realization of such power amplifiers are analyzed. A switch-mode realization is generally desired because it features a significantly higher efficiency compared to traditional analog realizations. However, the achievable Bandwidth (BW) in switch-mode amplifiers is ultimately limited by the maximum possible switching frequency. This frequency has to be chosen sufficiently higher than the corner frequency of the output filter. Therefore, series- and parallel-interleaving concepts are investigated to allow an effective switching frequency $f_{sw,eff}$ (relevant for filtering) in the MHz range despite a moderate switching frequency f_{sw} of the individual switches. Series-interleaving distributes the blocking voltage stress and parallel interleaving the current stress between multiple devices. Therefore, the combination of both approaches, i.e., the parallel-interleaved operation of several series-interleaved (multi-level) bridge-legs, is comprehensively analyzed in terms of loss, volume and design complexity scaling and eventually a Three-Level Triple-Interleaved (3L3) Flying Capacitor Converter (FCC) is selected. A highly compact hardware demonstrator (power density of 25 kW/dm³ / 410 W/in³) of a single-phase module is realized for performance verification. Important design aspects are described in detail. Experimental results verify the operation with 10 kVA output power (per phase) at 230 V rms output voltage with an output frequency of 100 kHz (nominal operating point), where a system efficiency of 95.8% and excellent output voltage quality (3rd and 5th harmonic 2.5 V

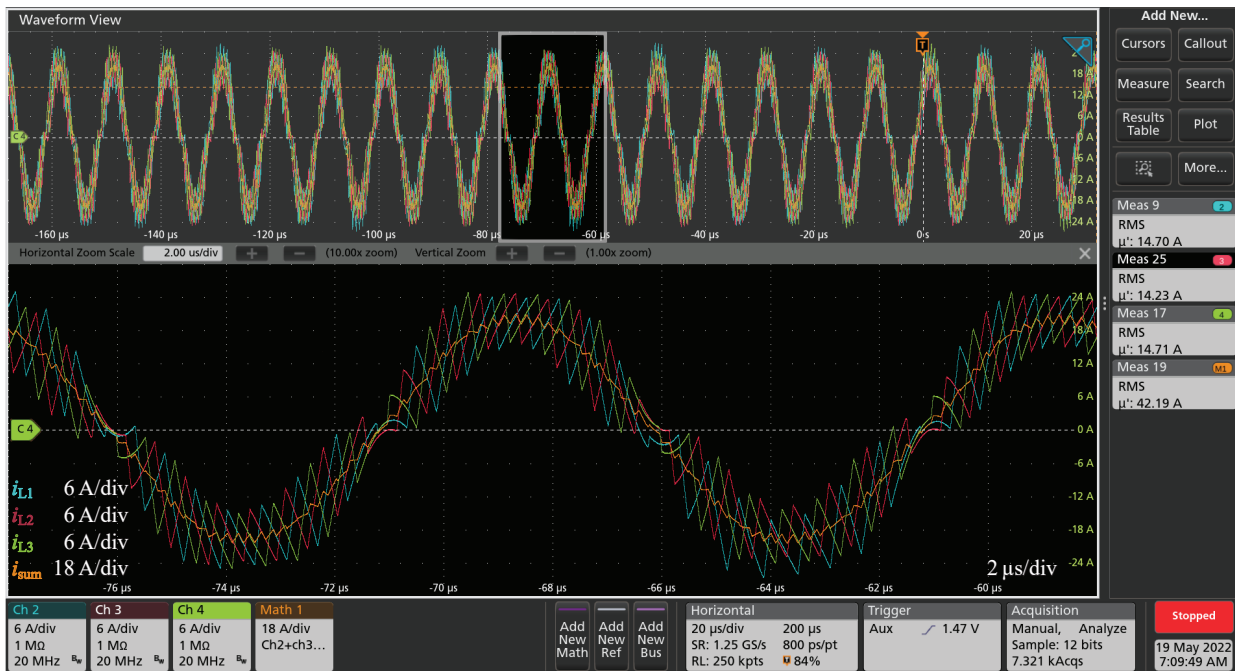


Fig. 15. Measured branch inductor currents i_{L1} (blue), i_{L2} (red) and i_{L3} (green) on a scale of 6 A/div indicating balanced current sharing between the three branches. Additionally, i_{sum} (orange, 18 A/div) indicates the reduced current ripple thanks to the parallel interleaving.

and 1.2 V, respectively) is achieved. A three-phase output can be realized with three individual single-phase modules of the presented converter or alternatively, the three parallel-interleaved branches of a 3L3 converter can be reconfigured for a three-phase output.

The presented versatile UHBW-PA module serves as a solid basis for testing and characterization of future power converters with WBG semiconductors. Further work on this topic includes the implementation of highly dynamic closed-loop controllers for different application scenarios, e.g., general amplification, virtual impedance emulation, machine emulation and so on. Important characterization parameters are then dynamic specifications such as the responses to a reference voltage step and to a load step (disturbance). Thereby, also a High-Resolution Pulse Width Modulation (HRPWM) and dead time correction are advantageously implemented to additionally improve the output voltage quality and/or to achieve high precision reference tracking.

APPENDIX A THEORETICAL PERFORMANCE LIMITATION

This appendix describes the output power limitations/derating for different load types, i.e., load phase angles. This derivation has already been presented in [10] and is included here for completeness. Given the sinusoidal nature of the output voltage and current, theoretical output power limitations for the proposed converter can directly be derived using the phasor representation of output voltage and current (cf. phasor diagram in **Fig. 3 (a.ii)**). For the nominal operating point at $f_{out} = 100$ kHz and $V_{out} = 230$ V rms, the theoretical possible apparent output power S_{Lim} for each load phase angle φ (phase-shift between

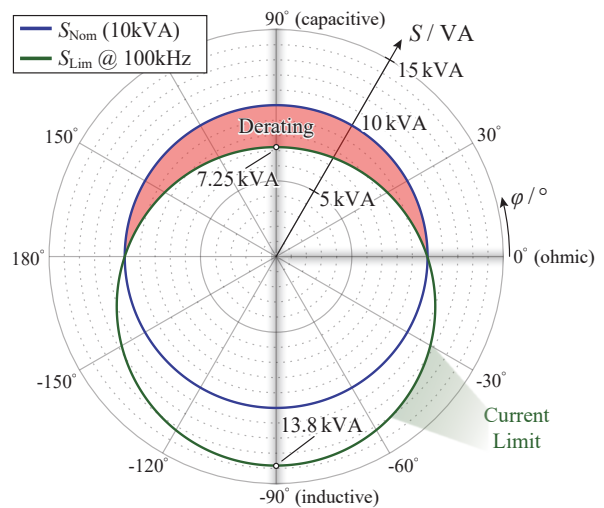


Fig. 16. Theoretical limitation S_{Lim} (green) of the apparent output power versus the load phase angle φ (phase-shift between the output voltage and current waveforms) for the given selection of the filter elements ($L_{filt} = 1.26$ μ H, $C_{filt} = 99$ nF) for a 100 kHz sinusoidal output signal with 230 Vrms relative to a nominal output power of 10 kVA (blue) and ohmic load ($\varphi = 0^\circ$). The limitation is derived from the switch rms current for $M = 3$ and $N = 3$ under the assumption of a worst-case peak-to-peak current ripple of 100 % (with respect to the fundamental component). The required derating of around 27.5 % of the output power for capacitive loads is highlighted in red; Figure based on [10].

output voltage and current waveforms) is depicted in **Fig. 16** in green. It is limited by two constraints:

- i) The maximum possible voltage amplitude that can be generated at the switch node, basically given by $V_{dc}/2$, here set to $0.95 \cdot V_{dc}/2$ to have a certain margin (corresponds to a modulation depth $m_M = 0.95$), i.e., $|v_{sw,eff}| \leq m_M \cdot V_{dc}/2$ according to the phasor diagram

in Fig. 3 (a.ii).

- ii) The maximum possible switch rms current, which is limited by the semiconductor losses and thus highly depends on the thermal design.

The rms current derived from the conduction losses occurring for $M = 3$ and $N = 3$ and ohmic load in the nominal operating point is taken as a reference (cf. Fig. 4 (a)), i.e., $I_{sw,rms} \approx 11.6$ A. The inductor current relates the switch current to the output current and its rms value is calculated under the assumption of a triangular peak-to-peak current ripple of 100 % (with respect to the amplitude of the fundamental component) as worst-case approximation. Since the current limit is derived from the ohmic load case, the S_{Lim} circle intersects with the blue circle representing the nominal power $S_{Nom} = 10$ kVA at $\varphi = 0^\circ$ and $\varphi = 180^\circ$. It is shown that for capacitive-resistive loads ($0^\circ < \varphi < 180^\circ$) the current limitation (constraint ii) in above list) leads to an output power derating of maximum 27.5 %, which is much lower compared to state-of-the-art linear power amplifiers (derating by a factor of three) [13]. For all other load cases, there is a sufficient margin, especially for inductive loads ($> 30\%$ margin) because they partially compensate the reactive power of the output filter. If higher currents would be allowed, the maximum possible converter voltage (constraint i) in above list) would limit the maximum output power for inductive loads ($\varphi = -90^\circ$), since in this case \underline{v}_{out} and \underline{v}_L are in phase (cf. Fig. 3 (a.ii)) and arithmetically add up to $\underline{v}_{sw,eff}$. This cannot be seen in Fig. 16 due to the strong current limit and because the inductance is chosen based on limiting the maximum inductor voltage to $k_v = 15\%$ of the peak output voltage for an ohmic load scenario.

REFERENCES

- [1] C. S. Edrington, M. Steurer, J. Langston, T. El-Mezyani, and K. Schoder, "Role of power hardware in the loop in modeling and simulation for experimentation in power and energy systems," *Proceedings of the IEEE*, vol. 103, no. 12, pp. 2401–2409, 2015.
- [2] F. Lehfuss, G. Lauss, P. Kotsampopoulos, N. Hatzigaryriou, P. Crolla, and A. Roscoe, "Comparison of multiple power amplification types for power hardware-in-the-loop applications," in *Proc. of the Complexity in Engineering (COMPENG)*, Aachen, Germany, Jun. 2012, pp. 1–6.
- [3] G. Lauss and K. Strunz, "Accurate and stable hardware-in-the-loop (hil) real-time simulation of integrated power electronics and power systems," *IEEE Transactions on Power Electronics*, vol. 36, no. 9, pp. 10920–10932, 2021.
- [4] K. Ma, J. Wang, X. Cai, and F. Blaabjerg, "Ac grid emulations for advanced testing of grid-connected converters—an overview," *IEEE Transactions on Power Electronics*, vol. 36, no. 2, pp. 1626–1645, 2021.
- [5] P. Jonke, J. Stoeckl, and H. Ertl, "Design and performance evaluation of a three phase ac power source with virtual impedance for validation of grid connected components," in *Proc. of the Power Electron. and Intell. Motion Conf. (PCIM Europe)*, Nuremberg, Germany, May 2016, pp. 1–7.
- [6] F. Krismer and J. W. Kolar, "Compensation and emulation of output impedance in ultra-high bandwidth class-d power amplifiers," in *Proc. of the 22nd IEEE Workshop on Control and Modelling of Power Electronics (COMPEL)*, Cartagena, Colombia, Nov. 2021, pp. 1–8.
- [7] M. Oetmeier, R. Bartelt, C. Heising, V. Staudt, A. Steimel, S. Tietmeier, B. Bock, and C. Doerlemann, "Power-electronic-based machine emulator for high-power high-frequency drive converter test," in *Proc. of the IEEE Vehicle Power and Propulsion Conference (VPPC)*, Lille, France, Sep. 2010, pp. 1–6.
- [8] A. Knop and F. W. Fuchs, "High frequency grid impedance analysis by current injection," in *Proc. of the 35th IEEE Annual Ind. Electron. Soc. Conf. (IECON)*, Porto, Portugal, Nov. 2009, pp. 536–541.
- [9] J. Sun, "Impedance-based stability criterion for grid-connected inverters," *IEEE Transactions on Power Electronics*, vol. 26, no. 11, pp. 3075–3078, 2011.
- [10] P. S. Niklaus, J. Azurza Anderson, D. Bortis, and J. W. Kolar, "Ultra-high bandwidth gan-based class-d power amplifier for testing of three-phase mains interfaces of renewable energy systems," in *Proc. of the 8th International Conference on Renewable Energy Research and Applications (ICRERA)*, Brasov, Romania, Nov. 2019, pp. 615–622.
- [11] J. Böhler, J. Huber, J. Wurz, M. Stransky, N. Uvaïdov, S. Srdic, and J. W. Kolar, "Ultra-high-bandwidth power amplifiers: A technology overview and future prospects," *IEEE Access*, vol. 10, pp. 54 613–54 633, 2022.
- [12] "7820 series," Datasheet, <https://aetechron.com/pdf/7820TechSpecs.pdf>, AE Techtron Inc., 2021, accessed: June 21st, 2022.
- [13] "Aps series of 4-quadrant amplifiers," Datasheet, <https://spitzenberger.de/web/1107>, Spitzenberger & Spies, 2021, accessed: June 21st, 2022.
- [14] "8500 series," Datasheet, <https://aetechron.com/pdf/8500TechSpecs.pdf>, AE Techtron Inc., 2022, accessed: June 21st, 2022.
- [15] "Compiso csu 200," Datasheet, https://www.egstonpower.com/wp-content/uploads/2020/04/Intro-COMPISO-SYSTEM-UNIT_Scalable-Power-Electronics-System.pdf, EGSTON Power Electronics, 2021, accessed: June 21st, 2022.
- [16] K. Zeng, S. Mao, G. Rietveld, J. Popovic, H. Yu, L. Wang, K. Liu, and Z. Zhou, "High-precision control method for high-power mri gradient power amplifiers," *IEEE Transactions on Power Electronics*, vol. 37, no. 8, pp. 9035–9046, 2022.
- [17] H. Sarnago, J. M. Burdío, T. García-Sánchez, L. M. Mir, I. Álvarez Gariburo, and O. Lucía, "Gan-based versatile waveform generator for biomedical applications of electroporation," *IEEE Access*, vol. 8, pp. 97 196–97 203, 2020.
- [18] L. Gómez, D. Serrano, and M. Vasic, "High-frequency modular multicell arbitrary waveform generator," in *Proc. of the IEEE Applied Power Electronic Conference and Exposition (APEC)*, Houston, TX, USA, Mar. 2022, pp. 1322–1328.
- [19] R. C. Beltrame, M. L. da Silva Martins, C. Rech, and H. L. Hey, "Hybrid power amplifiers - a review," in *Proc. of the XI Brazilian Power Electronics Conference (COBEP)*, Natal, Brazil, Sep. 2011, pp. 189–195.
- [20] R. Schwendemann, M. Lörcher, F. Sommer, L. Stefanski, and M. Hiller, "A new, universal series hybrid cascaded h-bridge converter for power-hardware in the loop emulation," in *Proc. of the 21st European Conference on Power Electronics and Applications (EPE ECCE Europe)*, Genova, Italy, Sep. 2019, pp. 1–10.
- [21] R. Schwendemann, M. Lörcher, and M. Hiller, "A new linear power amplifier for a series hybrid cascaded h-bridge converter used as a power hardware in the loop emulator," in *Proc. of the Power Electron. and Intelligent Motion Conf. (PCIM Europe)*, Virtual Conference, Jul. 2020, pp. 1–8.
- [22] H. Ertl, J. Kolar, and F. Zach, "Basic considerations and topologies of switched-mode assisted linear power amplifiers," *IEEE Transactions on Industrial Electronics*, vol. 44, no. 1, pp. 116–123, 1997.
- [23] L. Stefanski, D. Bernet, M. Schnarrenberger, C. Rollbühler, A. Liske, and M. Hiller, "Cascaded h-bridge based parallel hybrid converter — a novel topology for perfectly sinusoidal high power voltage sources," in *Proc. of the 45th IEEE Annual Ind. Electron. Soc. Conf. (IECON)*, Lisbon, Portugal, Oct. 2019, pp. 1639–1646.
- [24] —, "Cascaded h-bridge based parallel hybrid converter — a new voltage source for power-hardware-in-the-loop emulation systems," in *Proc. of the 21st IEEE Workshop on Control and Modelling of Power Electronics (COMPEL)*, Aalborg, Denmark, Nov. 2020, pp. 1–8.
- [25] S. Kashiwagi, "A high-efficiency audio power amplifier using a self-oscillating switching regulator," *IEEE Transactions on Industry Applications*, vol. 21, no. 4, pp. 906–911, 1985.
- [26] V. Yousefzadeh, E. Alarcon, and D. Maksimovic, "Three-level buck converter for envelope tracking in rf power amplifiers," in *Proc. of the IEEE Applied Power Electronic Conference and Exposition (APEC)*, vol. 3, Austin, TX, USA, Mar. 2005, pp. 1588–1594.
- [27] —, "Three-level buck converter for envelope tracking applications," *IEEE Transactions on Power Electronics*, vol. 21, no. 2, pp. 549–552, 2006.
- [28] G. Gong, H. Ertl, and J. W. Kolar, "Novel tracking power supply for linear power amplifiers," *IEEE Transactions on Industrial Electronics*, vol. 55, no. 2, pp. 684–698, 2008.
- [29] T. A. Meynard and G. Fontes, "Design methods and tools for power electronics," *Tutorial presented at the Power Electron. and Intelligent Motion Conf. (PCIM Europe)*, Nuremberg, Germany, pp. 1–218, may 2019.
- [30] D. G. Holmes and T. Lipo, *Pulse Width Modulation for Power Converters: Principles and Practice*, 1st ed. United States of America: John Wiley & Sons, 2003.
- [31] J. Ertl, "Schaltverstärker mit hoher Ausgangsspannungsqualität: Konzepte - Eigenschaften - Anwendungen (in German)," Habilitation, Technische Universität Wien, Vienna, Austria, 2003.
- [32] J. Azurza Anderson, G. Zulauf, J. W. Kolar, and G. Deboy, "New figure-of-merit combining semiconductor and multi-level converter properties," *IEEE Open Journal of Power Electronics*, vol. 1, pp. 322–338, 2020.
- [33] A. Lesnicar and R. Marquardt, "A new modular voltage source inverter topology," in *Proc. of the 10th Europ. Power Electron. and Appl. Conf. (EPE)*, Toulouse, France, Sep. 2003, pp. 1–10.

- [34] L. Ångquist, A. Antonopoulos, D. Siemaszko, K. Ilves, M. Vasiladiotis, and H.-P. Nee, "Open-loop control of modular multilevel converters using estimation of stored energy," *IEEE Transactions on Industry Applications*, vol. 47, no. 6, pp. 2516–2524, 2011.
- [35] W. McMurray, "Fast response stepped-wave switching power converter circuit," U.S. Patent 3,581,212, May 1971.
- [36] R. H. Baker, "Bridge converter circuit," U.S. Patent 4,270,163, May 1981.
- [37] J. Rodriguez, J.-S. Lai, and F. Z. Peng, "Multilevel inverters: a survey of topologies, controls, and applications," *IEEE Transactions on Industrial Electronics*, vol. 49, no. 7, pp. 724–738, 2002.
- [38] T. A. Meynard and H. Foch, "Multi-level conversion: High voltage choppers and voltage-source inverters," in *Proc. of the 23rd Annual IEEE Power Electronics Specialists Conference (PESC)*, Toledo, Spain, Jun. 1992, pp. 397–403.
- [39] R. H. Wilkinson, T. A. Meynard, and H. du Toit Mouton, "Natural balance of multicell converters: The general case," *IEEE Transactions on Power Electronics*, vol. 21, no. 6, pp. 1658–1666, Nov 2006.
- [40] Y. Lei, C. Barth, S. Qin, W. Liu, I. Moon, A. Stillwell, D. Chou, T. Foulkes, Z. Ye, Z. Liao, and R. C. N. Pilawa-Podgurski, "A 2-kw single-phase seven-level flying capacitor multilevel inverter with an active energy buffer," *IEEE Transactions on Power Electronics*, vol. 32, no. 11, pp. 8570–8581, Nov 2017.
- [41] C. B. Barth, T. Foulkes, W. H. Chung, T. Modeer, P. Assem, P. Assem, Y. Lei, and R. C. N. Pilawa-Podgurski, "Design and control of a gan-based, 13-level, flying capacitor multilevel inverter," in *Proc. of the 17th IEEE Workshop on Control and Modeling for Power Electronics (COMPEL)*, Trondheim, Norway, Jun. 2016, pp. 1–6.
- [42] M. Gleissner and M. M. Bakran, "Design and control of fault-tolerant nonisolated multiphase multilevel dc-dc converters for automotive power systems," *IEEE Transactions on Industry Applications*, vol. 52, no. 2, pp. 1785–1795, 2016.
- [43] G. Stanley and K. Bradshaw, "Precision dc-to-ac power conversion by optimization of the output current waveform—the half bridge revisited," *IEEE Transactions on Power Electronics*, vol. 14, no. 2, pp. 372–380, 1999.
- [44] J. Li, C. Sullivan, and A. Schultz, "Coupled-inductor design optimization for fast-response low-voltage dc-dc converters," in *Proc. of the IEEE Applied Power Electronic Conference and Exposition (APEC)*, vol. 2, Dallas, TX, USA, Mar. 2002, pp. 817–823.
- [45] D. H. Zhou, J. Celikovic, Y. Elasser, D. Maksimovic, and M. Chen, "Balancing limits of flying capacitor voltages in coupled inductor fcm1 converters," in *Proc. of the 23rd IEEE Workshop on Control and Modeling for Power Electronics (COMPEL)*, Tel Aviv, Israel, Jun. 2022, pp. 1–8.
- [46] D. O. Boillat, T. Friedli, J. Mühlethaler, J. W. Kolar, and W. Hribernik, "Analysis of the design space of single-stage and two-stage lc output filters of switched-mode ac power sources," in *Proc. of the IEEE Power and Energy Conference at Illinois (PECI)*, Champaign, IL, USA, Feb. 2012, pp. 1–8.
- [47] "Igot60r070d1 - 600v coolgan enhancement-mode power transistor," Datasheet, https://www.infineon.com/dgdl/Infineon-IGOT60R070D1-DataSheet-v02_14-EN.pdf?fileId=5546d46265f064ff016685fa65066523, Infineon Technologies AG, 2021, accessed: June 14th, 2022.
- [48] B. Guenin, "Thermal vias - a packaging engineer's best friend," Online, <https://www.electronics-cooling.com/2004/08/thermal-vias-a-packaging-engineers-best-friend/>, Electronics Cooling, 2004, accessed: June 14th, 2022.
- [49] G. Langer, M. Leitgeb, J. Nicolics, M. Unger, H. Hoschopf, and F. P. Wenzl, "Advanced thermal management solutions on pcbs for high power applications," *Journal of Microelectronics and Electronic Packaging*, vol. 11, no. 3, pp. 104–114, 2014.
- [50] Y. Uemoto, M. Hikita, H. Ueno, H. Matsuo, H. Ishida, M. Yanagihara, T. Ueda, T. Tanaka, and D. Ueda, "Gate injection transistor (git)—a normally-off algan/gan power transistor using conductivity modulation," *IEEE Transactions on Electron Devices*, vol. 54, no. 12, pp. 3393–3399, 2007.
- [51] "Gs66506t - top-side cooled 650v e-mode gan transistor," Datasheet, <https://gansystems.com/wp-content/uploads/2020/04/GS66506T-DS-Rev-200402.pdf>, GaN Systems, 2020, accessed: Sept. 7th, 2022.
- [52] "Gs66516t - top-side cooled 650v e-mode gan transistor," Datasheet, <https://gansystems.com/wp-content/uploads/2021/10/GS66516T-DS-Rev-210727.pdf>, GaN Systems, 2021, accessed: Sept. 7th, 2022.
- [53] R. Hou and J. Lu, "The effect of dynamic on-state resistance to system losses in gan-based hard-switching applications," in *Proc. of the Power Electron. and Intell. Motion Conf. (PCIM Europe)*, Nuremberg, Germany, May 2019, pp. 1–7.
- [54] S. Kaneko, M. Kuroda, M. Yanagihara, A. Ikoshi, H. Okita, T. Morita, K. Tanaka, M. Hikita, Y. Uemoto, S. Takahashi, and T. Ueda, "Current-collapse-free operations up to 850 v by gan-git utilizing hole injection from drain," in *Proc. of the 17th Internat. Symp. on Power Semico. Dev. & ICs (IPSD)*, Hong Kong, China, May 2015, pp. 41–44.
- [55] J. Sun, O. Haebleren, C. Ostermaier, G. Pechtl, R. Tadikonda, E. Persson, R. Garg, M. Imam, S. Khalil, and A. Charles, "Dynamics of hole injection from p-gan drain of a hybrid drain embedded git," *AIP Advances*, vol. 11, no. 5, p. 055101, 2021.
- [56] M. Kasper, R. M. Burkart, G. Deboy, and J. W. Kolar, "Zvs of power mosfets revisited," *IEEE Transactions on Power Electronics*, vol. 31, no. 12, pp. 8063–8067, 2016.
- [57] B. Zojer, "Driving coolgan 600v coolgan high electron mobility transistors," Application Note, https://www.infineon.com/dgdl/Infineon-ApplicationNote_CoolGaN_600V_emode_HEMTs_Driving_CoolGaN_high_electron_mobility_transistors_with_EiceDRIVER_1EDI_Compact-ApplicationNotes-v02_00-EN.pdf?fileId=5546d46262b31d2e016368e4d7a90708, Infineon Technologies AG, 2018, accessed: June 14th, 2022.
- [58] D. Cittanti, E. Vico, and I. R. Bojoi, "New fom-based performance evaluation of 600/650 v sic and gan semiconductors for next-generation ev drives," *IEEE Access*, vol. 10, pp. 51 693–51 707, 2022.
- [59] C. W. T. McLyman, *Transformer and Inductor Design Handbook*, 3rd ed. New York, United States of America: CRC Press, 2004.
- [60] J. Biela, "Optimierung des elektromagnetisch integrierten serien-parallel Resonanzkonverters mit eingepprägtem Ausgangsstrom (in German)," Ph.D. dissertation, ETH Zurich, Zürich, Switzerland, 2005.
- [61] M. Mu, Q. Li, D. J. Gilham, F. C. Lee, and K. D. T. Ngo, "New core loss measurement method for high-frequency magnetic materials," *IEEE Transactions on Power Electronics*, vol. 29, no. 8, pp. 4374–4381, 2014.
- [62] D. Bortis, O. Knecht, D. Neumayr, and J. W. Kolar, "Comprehensive evaluation of gan git in low- and high-frequency bridge leg applications," in *Proc. of the 8th IEEE International Power Electronics Motion Control Conference (IPEMC-ECCE Asia)*, Hefei, China, May 2015, pp. 21–30.
- [63] U. Scheuermann, "Heat: Basics, examples, heat-exchange part 2," *ECPE Tutorial "Thermal Engineering of Power Electronic Systems" Part I*, Semikron Elektronik GmbH & Co. KG, Nuremberg, pp. 1–41, 2015.
- [64] F. Krismer, V. N. Behrunani, P. S. Niklaus, and J. W. Kolar, "Optimized cascaded controller design for a 10 kw / 100 khz large signal bandwidth ac power source," in *Proc. of the IEEE Energy Conversion Congress and Exposition (ECCE)*, Detroit, MI, USA, Oct. 2020, pp. 5669–5676.
- [65] P. S. Niklaus, D. Bortis, and J. W. Kolar, "High bandwidth high cmrr current measurement for a 4.8 mhz multi-level gan inverter ac power source," in *Proc. of the IEEE Applied Power Electronic Conference and Exposition (APEC)*, Phoenix, AZ, USA, Jul. 2021, pp. 200–207.
- [66] P. S. Niklaus, D. Bortis, and J. W. Kolar, "Beyond 50 mhz bandwidth extension of commercial dc-current measurement sensors with ultra-compact pcb integrated pickup coils," *IEEE Transactions on Industry Applications*, vol. 58, no. 4, pp. 5026–5041, 2022.
- [67] T. A. Meynard and H. Foch, "Multi-level choppers for high voltage applications," *EPE Journal*, vol. 2, no. 1, pp. 45–50, 1992.
- [68] D. M. Mitchell, "Pulsewidth modulator phase shift," *IEEE Transactions on Aerospace and Electronic Systems*, vol. AES-16, no. 3, pp. 272–278, 1980.
- [69] C. Wu, W.-H. Lau, and H. Shu-Hung Chung, "Analytical technique for calculating the output harmonics of an h-bridge inverter with dead time," *IEEE Transactions on Circuits and Systems I: Fundamental Theory and Applications*, vol. 46, no. 5, pp. 617–627, 1999.
- [70] F. Chierchie, L. Stefanazzi, E. E. Paolini, and A. R. Oliva, "Frequency analysis of pwm inverters with dead-time for arbitrary modulating signals," *IEEE Transactions on Power Electronics*, vol. 29, no. 6, pp. 2850–2860, 2014.
- [71] F. Chierchie, E. E. Paolini, and L. Stefanazzi, "Dead-time distortion shaping," *IEEE Transactions on Power Electronics*, vol. 34, no. 1, pp. 53–63, 2019.



Pascal S. Niklaus (STM'17) received his B.Sc. and M.Sc. degree (with distinction) in electrical engineering from the Swiss Federal Institute of Technology (ETH) Zurich, Switzerland, in 2016 and 2018, respectively. During his studies he did two internships where he developed hardware, firmware and software for custom and off-the-shelf test and measurement equipment with daugon AG, Dietikon, Switzerland as well as working on the firmware development for a new microprocessor architecture with ACP AG, Zurich, Switzerland. In April 2018 he joined the Power Electronic Systems Laboratory (PES) at ETH Zurich as a doctoral student focusing on advanced measurement technologies in the field of power electronics and on high bandwidth power converters featuring wide bandgap power semiconductors.



Johann W. Kolar (F'10) received his M.Sc. and Ph.D. degree (summa cum laude) from the University of Technology Vienna, Austria, in 1997 and 1999, respectively. Since 1984, he has been working as an independent researcher and international consultant in close collaboration with the Vienna University of Technology, in the fields of power electronics, industrial electronics and high performance drive systems. He was appointed Assoc. Professor and Head of the Power Electronic Systems Laboratory at the Swiss Federal Institute of Technology (ETH) Zurich on Feb. 1, 2001, and was promoted

to the rank of Full Prof. in 2004. Dr. Kolar has proposed numerous novel converter concepts incl. the Vienna Rectifier, the Sparse Matrix Converter and the Swiss Rectifier, has spearheaded the development of x-million rpm motors, and has pioneered fully automated multi-objective power electronics design procedures. He has graduated 80+ Ph.D. students, has published 1000+ journal and conference papers and 4 book chapters, and has filed 200+ patents. He has presented 30+ educational seminars at leading international conferences and has served as IEEE PELS Distinguished Lecturer from 2012 – 2016. He has received 40+ IEEE Transactions and Conference Prize Paper Awards, the 2014 IEEE Power Electronics Society R. David Middlebrook Achievement Award, the 2016 IEEE PEMC Council Award, the 2016 IEEE William E. Newell Power Electronics Award, the 2021 EPE Outstanding Achievement Award and 2 ETH Zurich Golden Owl Awards for excellence in teaching. He is a Fellow of the IEEE and was elected to the U.S. National Academy of Engineering as an international member in 2021. The focus of his current research is on ultra-compact/efficient WBG converter systems, ANN-based design procedures, Solid-State Transformers, ultra-high speed drives, bearingless motors, and life cycle analysis of power electronics converter systems.



Dominik Bortis (SM'21) received the M.Sc. and Ph.D. degree in electrical engineering from the Swiss Federal Institute of Technology (ETH) Zurich, Switzerland, in 2005 and 2008, respectively. In May 2005, he joined the Power Electronic Systems Laboratory (PES), ETH Zurich, as a Ph.D. student. From 2008 to 2011, he has been a Postdoctoral Fellow and from 2011 to 2016 a Research Associate with PES. Since January 2016 Dr. Bortis is heading the research group Advanced Mechatronic Systems at PES, which concentrates on ultra-high speed motors, bearingless drives, linear-rotary actuator and

machine concepts with integrated power electronics. Targeted applications include e.g. highly dynamic positioning systems, medical systems, and future mobility concepts. Dr. Bortis has published 90+ scientific papers in international journals and conference proceedings. He has filed 30+ patents and has received 10 IEEE Conference Prize Paper Awards and 2 First Prize Transaction Paper Awards.